PHYSICAL REVIEW C VOLUME 43, NUMBER 2 FEBRUARY 1991

Time scales for binary fragmentations of highly excited, fissile nuclei from $^{32}S + ^{197}Au$, ^{232}Th

E. Mordhorst, M. Strecker, H. Frobeen, M. Gasthuber, and W. Scobel
Universität Hamburg, I. Institut für Experimentalphysik, D-2000 Hamburg 50, Federal Republic of Germany

B. Gebauer, D. Hilscher, M. Lehmann, H. Rossner, and Th. Wilpert
Hahn-Meitner-Institut Berlin, D-1000 Berlin 39, Federal Republic of Germany

(Received 19 July 1990)

Fission of ^{197}Au,^{232}Th + 838-MeV ^{32}S projectiles was studied by measuring fragment coincident neutrons. Neutron energy spectra were decomposed into preequilibrium, prescission, and postscission contributions with a constrained moving source analysis. Excitation energies deduced from the transferred linear momentum are consistent with calculations applying the Boltzmann master equation, and with an energy balance based upon the experimental neutron multiplicities and charged particles from evaporation calculations. The time scale of fission derived from the prescission neutron multiplicities extends from 5×10^{-21} to 3×10^{-20} s; it does not depend on the initial excitation energy, is about a factor of 2 longer for symmetric than for asymmetric fragmentations, and increases with the fissility of the primary reaction system. For all mass splits, the excitation energy left at scission is 50–60 MeV.

I. INTRODUCTION

Binary fission of an excited nuclear reaction system is a process involving collective degrees of freedom and therefore considered to be inherently slower than interactions coupling only nucleon degrees of freedom. This difference may result in a delay that becomes experimentally accessible under favorite experimental conditions. Growing evidence has indeed been found for such a delay by using the enhanced neutron[1,2] or charged particle[3] emission or γ decay modes[4] preceding or competing with[5] fission. In particular, prescission neutron multiplicities have been introduced in recent years as a clock for the dynamical fission time scale over a broad range of primary excitation energies.[2,6,7,15]

Conceptionally, one can distinguish between three subsequent time intervals contributing to the scission time scale,[1,2,8,9] namely the equilibration time for compound nucleus formation τ_{PE}, the transient time τ_t to reach a quasistationary probability flow across the saddle point for an irreversible development towards scission, and the saddle-to-scission time τ_{ss} to proceed to the scission configuration.

Calculations with the Boltzmann master equation (BME) model show[10] that the equilibration phase for reactions with 10–100 MeV/u projectiles ^{27}Al extends to typically 5×10^{-22} s with little dependence on the injection mechanism;[11] similarly, Landau-Vlasov simulations indicate[12,44] that the fractional linear momentum transfer (LMT) is completed after this time. For nuclei with a nonvanishing fission barrier, a nuclear dissipation mechanism must couple the fission degrees of freedom to the intrinsically equilibrated reaction system. The rate of this dissipation corresponds to a fairly strong nuclear viscosity such that the motion towards scission is overdamped;[2,9] the times τ_t and τ_{ss} obtained in Refs. 9 and 13 for $^{16}O + ^{142}Nd$ at 207 MeV are in the order of 6×10^{-21} s and $2\text{–}4\times10^{-21}$ s, respectively, and are expected to show only little dependence on mass number A.[9,14,15]

Neutron multiplicity experiments separating the prescission multiplicity M_{pre} from those of the fragments, M_{post}, by means of the different kinematical focusing of the respective moving sources yield only the sum $\tau_t + \tau_{ss}$; for heavy systems ($A \geq 200$) values in the order of 10^{-20} s are anticipated[8,16] and thus the emission during transition from equilibrium deformation to scission is likely to dominate.[15]

Whereas absolute values for $\tau_t + \tau_{ss}$ deduced with the neutron clock may be affected by systematic errors of factors two or more due to, e.g., uncertainties in the level densities applied or the initial equilibrium shape at maximum excitation, they allow more precise comparisons on a relative scale. Emphasis will be put on the question of whether or not the sum $\tau_t + \tau_{ss}$ is dependent (i) on the fissility x of the reaction system, (ii) on the initial excitation energy, and (iii) on the fragment mass split.

As far as (i) is concerned, there are different trends observed or predicted. Newton *et al.*[15] give arguments that τ_{ss} will dominate and will increase with x for one body dissipation and for two body viscosity.[16] In Ref. 1 assuming emission from the equilibrium configuration only, an increase of the prescission time $\tau_t + \tau_{ss}$ from 3×10^{-20} s (for $x \approx 0.6$) to 2×10^{-19} s (for $x \approx 0.85$) was found. On the other hand, the same data show a different trend for extreme assumptions of pure saddle-point or saddle-to-scission neutron emission, suggesting that the fission time scale should be almost independent of fissility.[2] It is therefore mandatory to perform a consistent neutron-clock analysis for data to be compared. In this work we will convert the prescission multiplicities M_{pre} observed in binary fragmentations of the reaction systems $^{32}S + ^{197}Au$,^{232}Th with 838-MeV projectiles into the *minimum* time $\tau_{ss} + \tau_t$ required to explain the value M_{pre} observed by assuming *no* statistical competition of fission with particle evaporation from the equilibrium deformation.

The questions (i)–(iii) raised demand the knowledge of the excitation energy E_{CN}^* deposited in the system later undergoing fission, and of the fragment masses as well. Beyond that, the determination of the energy and linear momentum transferred from the projectile to the reaction system is of actual interest in its own, because it (iv) allows us to test LMT systematics predicting a saturation on a per nucleon basis even for the most dissipative collisions when projectile energies of 30 MeV/u are approached;[17,18] (v) is a prerequisite for a study of prescission neutron multiplicity versus total kinetic energy (TKE) of the fragments, where unexpected behavior has recently been reported.[2,19]

In addition, the excitation energies E_{CN}^*(LMT) must be confronted with the respective nuclear temperatures T observed for the prescission neutron sources to yield a consistent level-density parameter for the neutron-clock analysis.

In the present work, E_{CN}^* was determined from the LMT measured with the folding angle technique and with the kinematics of a massive transfer process. In order to justify this method and to allow a broad range of excitation energies to be sampled, the experimental conditions had to be chosen to yield the maximum possible excitation energy compatible with a dominance of binary fission, and to enhance selectivity for the binary component with an appropriate (i.e., planar) detector geometry.

The reaction systems ^{32}S+^{197}Au,^{232}Th with 838-MeV projectile energies allow us to extend the fissility range from[6] $x=0.65$ for ^{32}S+^{144,154}Sm to $x=0.90$; for projectile energies per nucleon of $\epsilon=26.2$ MeV/u average LMT values of 80% can be expected[10,20] with excitation energies E_{CN}^* of almost 500 MeV and nuclear temperatures of up to 4 MeV.[12,21] At the same time, intermediate mass fragment (IMF) contributions should stay below 20% in measurements with 4π geometry[22] and be much smaller for planar reaction geometry. The assumption of a dominantly binary fragmentation is supported by experiments[21–25] and model calculations for ^{40}Ar+^{197}Au at 27.2 MeV/u, but needs its own justification for the systems under study before the questions (i)–(v) can be adequately addressed.

The paper is organized as follows: In Sec. II the experimental setup will be explained, followed (Sec. III) by a discussion of fission fragment analysis and the extent of binary fragmentation. Section IV is then devoted to a moving source decomposition of the fission coincident neutrons, and the interpretation of preequilibrium (PE), prescission, and postscission source parameters. Statistical model calculations presented in Sec. V provide the basis for the determination of scission time scales. We conclude with a short summary.

II. EXPERIMENTAL METHODS

A. Setup

The experiment was performed with the ^{32}S beam from the VICKSI accelerator at the Hahn-Meitner-Institut with a laboratory energy of 838 MeV or 26.2 MeV/u, a linear momentum $p_0=7090$ MeV/c or 222 MeV/c u, and a repetition rate $\nu_{\mathrm{RF}}=18.63$ MHz. The targets of thickness 300 μg/cm^2 (^{197}Au, self-supporting) and 290 μg/cm^2 (^{232}ThF$_4$ on 30 μg/cm^2 carbon foil) were mounted inside a thin walled (3 mm stainless steel) scattering chamber with 50 cm radius and 70 cm height, with a high voltage of +18 kV applied to prevent a loading of the detectors with secondary electrons released by the beam.

Inside this chamber, the detector setup (cf. Fig. 1) consisted of a position-sensitive low-pressure multiwire chamber (MWC) of active size 244×122 mm^2 on one side of the beam in a minimum distance of 272 mm from the target, and a set of four equally spaced (12°) surface barrier detectors $F1$–$F4$ (thickness 170 μm, distances 20–22 cm, angular acceptances $\Delta\phi=\pm4°$, $\Delta\theta=\pm3°$, corresponding to a solid angle of 13 msr). The detectors $F1$–$F4$ could be shifted jointly by 6° such that the angular range covered in the reaction plane was $\theta=35°$–$83°$ ($\theta=36°$–$84°$) on the MWC ($F1$–$F4$) side. The angular acceptance of the MWC out of plane was $\Delta\phi=\pm12°$. By measuring both positions and the time of flight (TOF) on the MWC side (spatial resolution $\sigma_{x,y}=0.35$ mm, time resolution $\sigma_t\approx100$ ps) and the TOF ($\sigma_{t,F}=140$ ps) as well as the pulse height on the $F1$–$F4$ side, these detectors were used for reconstruction of kinematic coincidences between fragment-like reaction products. The setup was centered at the angles $\theta_{\mathrm{MWC}}\approx\theta_F\approx59°$ corresponding to 75% LMT in symmetric binary fragmenta-

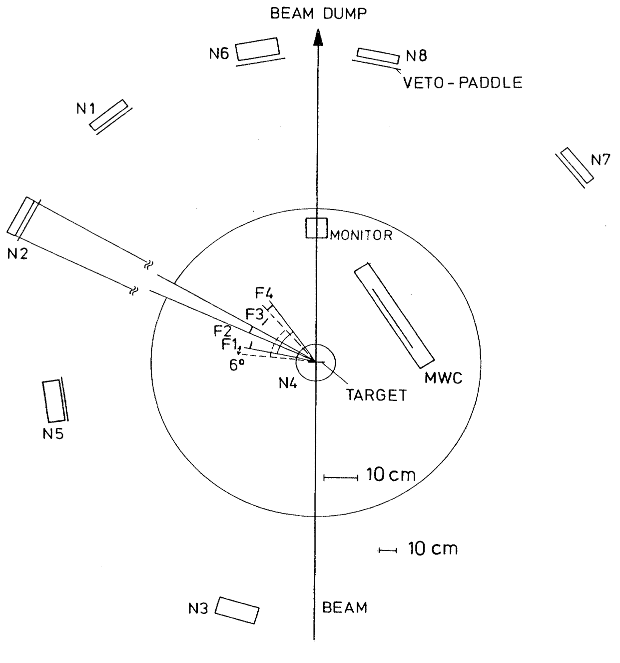

FIG. 1. Schematic diagram of the experimental setup consisting of neutron detectors $N1$–$N8$ (partly with a veto paddle in front), a position sensitive multiwire proportional chamber MWC, and solid state detectors $F1$–$F4$ for fragment detection. The elastic scattering monitors $M1$,$M2$ under 0° are ±8° off plane. For further details, see text.

tions. Angle calibration of the MWC was performed with slit masks as described in Ref. 19. For the pulse-height calibration of the Si detectors a ^{252}Cf source was repeatedly brought into the target position during the experiment; the pulse-height defect was accounted for following the prescription of Schmitt *et al.*[26] with the parameter values adopted[28] from Weissenberger *et al.*[27] Energy losses of fission fragments in the target were accounted for as described in Refs. 7 and 29. The absolute time scale for the determination of the fragment velocities v_1, v_2 on all five ($F1$–$F4$, MWC) TOF arms was accomplished by selecting symmetric fragmentations with the TKE known from the pulse height measured with the solid state detector.[7,30] The resulting time resolution was determined by the contributions from the burst width and (for $F1$–$F4$) by the plasma delay correction[29] and leads to a typical uncertainty in the velocity component $v_\parallel$ of the composite system in projectile direction of $\sigma_{v_\parallel} \approx 0.06 v_\parallel$. The resulting uncertainties of the LMT and the fragment mass [cf. Eqs. (2) and (3) in Sec. III A] are $\sigma_m \approx 0.06m$ and $\sigma_{\text{LMT}} \approx 0.06$ LMT, respectively, with a general tendency to higher uncertainties for small LMT values.[30,31] It is worth stressing that the determination of the absolute time scale from symmetric fragmentations yielded similar velocity distributions on the $F1$–$F4$ and the MWC side not only for these events, but also for the asymmetric fragmentations correlating different fragment detectors F_i via the corresponding regions on the MWC side as is demonstrated in Fig. 2. The velocities of a fission coincidence are therefore mutually consistent.

The beam position was monitored with two small scintillators NE102A under 0°, but ±8° off the reaction plane. Elastically scattered projectiles were used to determine the burst width (850±20 ps FWHM) and provided the beam intensity of approximately 1 particle nA for cross section normalization purposes.

Eight neutron TOF detectors consisting of cylindrical cells (diameter 25.4 cm) filled with the liquid scintillator NE213 or BC501 were positioned in TOF distances varying between 80 and 220 cm, cf. Table I. All but two ($N3$,$N4$) were equipped with scintillator Veto paddles for discrimination against energetic charged ejectiles, and all had a front cover of 3 mm Pb for suppression of low energy γ radiation. Pulse-shape and TOF informations were used for $n\gamma$ discrimination. The neutron flux attenuation by construction materials was calculated with the code[32] ATTENE as a function of neutron energy. The neutron detector efficiencies $\eta\ (E_n^{\text{th}}, E_n)$ were calculated with the code[33] NEFF4 for $E_n < 20$ MeV; above, the one of Ref. 34 was applied. Further details were discussed elsewhere.[31] The estimated uncertainties of the efficiency ($\leq 8\%$), the absorption correction ($\leq 10\%$), and the background subtraction ($\leq 10\%$) yield an overall uncertainty for the neutron TOF spectra of about 15%. Uncertainties pertinent to the parameters of the moving source fits are quoted in Sec. IV.

Data collection was triggered by a coincidence between the MWC and one of the detectors $F1$–$F4$; it generated a gate signal of width 50 ns identifying the corresponding Cyclotron RF signal for all TOF measurements including coincident neutron detectors. The random coincidences contribute less than 0.2%; this distortion was neglected. Occasionally single events from $F1$–$F4$ were recorded, too.

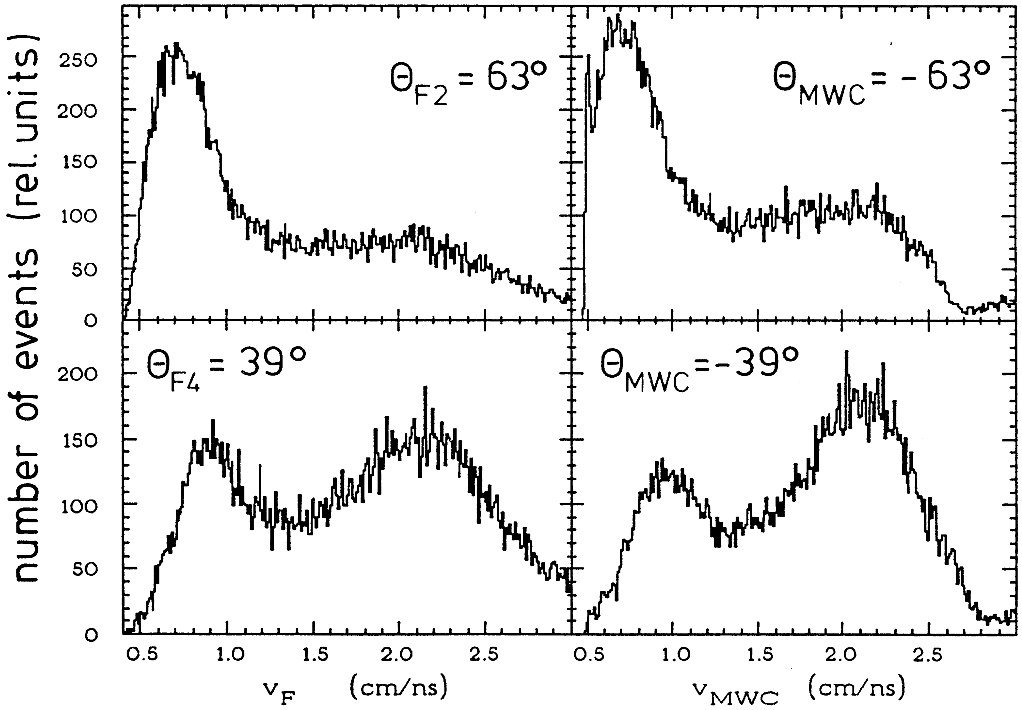

FIG. 2. Velocity spectra of coincident fragments detected with surface barrier detectors $F2$,$F4$ or with the MWC in the same angular range but at the opposite side of the beam.

TABLE I. Neutron detector features. ΔT is the time resolution (FWHM) for a software threshold set at $E_n=2$ MeV; detectors $N1,N2$ were shifted together with $F1$–$F4$ to be always aligned with $F4$ and $F2$.

Detector no.	θ (deg)	ϕ (deg)	TOF path (cm)	Thickness (cm)	Threshold $E_n^{\rm th}$ (MeV)	ΔT (ns)
$N1$	39 and 45	0	196.5	5.08	0.87	1.2
$N2$	63 and 69	0	192.5	5.08	0.76	1.3
$N3$	164	0	150.5	10.16	0.92	1.8
$N4$	90	90	80.5	10.16	0.92	1.7
$N5$	98	0	161.0	10.16	0.99	1.6
$N6$	11.5	0	217.5	10.16	1.00	1.5
$N7$	−39	0	191.0	5.08	1.00	1.5
$N8$	−11.5	0	220.0	5.08	0.98	1.3

III. FISSION FRAGMENT INTERPRETATION

A. Formalism

For the subsequent discussion a binary fragmentation following an (incomplete) fusion with the fractional LMT is assumed. From the folding angle $\theta_1+\theta_2$ and the fragment velocities v_1,v_2 of each event, the recoil velocity $v_\parallel$ of the composite system CN undergoing fission is calculated as[20]

$$v_\parallel=\frac{v_1 v_2 \sin(\theta_1+\theta_2)}{v_1\sin\theta_1+v_2\sin\theta_2} \tag{1}$$

and the fragment masses m_1,m_2 normalized to the mass m'_{CN} of the fissioning system at the scission point, m_N and $(1-m_N)$, as

$$m_N=\frac{m_1}{m'_{CN}}=\frac{1}{1+\dfrac{v_1\sin\theta_1}{v_2\sin\theta_2}} \; . \tag{2}$$

The fractional LMT ρ is defined with the projectile momentum $m_p \cdot v_p$ and the momentum components $p_{i\parallel}=m_i v_i \cos\theta_i$ as

$$\rho .=\frac{p_{1\parallel}+p_{2\parallel}}{m_p\cdot v_p} \; .$$

In the massive transfer model the spectator part of the projectile is assumed to follow the projectile trajectory with velocity v_p such that

$$\rho=\frac{v_\parallel}{v_0}\cdot\frac{1}{1+\dfrac{m_p}{m_T}\cdot\left[1-\dfrac{v_\parallel}{v_0}\right]} \; , \tag{3}$$

where v_0 denotes the velocity $v_\parallel$ for complete fusion and m_T is the target mass. The mass m'_{CN} is then given by

$$m'_{CN}=m_T+\rho m_p-m_{\rm evap} \; , \tag{4}$$

where $m_{\rm evap}$ is a correction of mass lost prior to the fragmentation by particle evaporation.

The LMT is associated with a corresponding excitation energy $E^*_{CN}(\rho)$ of the composite system, which may be written as[35]

$$E^*_{CN}(\rho)=E_{\rm trans}(\rho)+Q(\rho)-E_{\rm PE} \; , \tag{5}$$

with

$$E_{\rm trans}(\rho)=E_p\cdot\rho\cdot\frac{m_T}{m_T+\rho m_p}\cdot\sqrt{1-(v_p/c)^2} \; . \tag{6}$$

Here, E_p is the projectile energy in the laboratory system. The third term in Eq. (5) should account for the kinetic energy the PE neutrons of multiplicity $M_{\rm PE}$ and mass m_n carried away in excess of the amount $M_{\rm PE}(m_n/m_p)E_p$ already taken care of in the first term with the assumption that the spectator fraction $(1-\rho)m_p$ of the projectile moves on with beam velocity v_p. Different treatments of $E_{\rm PE}$ have been reported.[22,35–38] In view of the uncertainties due to the PE charged particle emission neglected in Eq. (5) and the width $\Delta\rho$ and ΔE^*_{CN} of the windows applied in the further data analysis, no such correction—that is estimated to represent at most a 10% effect[35]—is applied here. This omission will find further justification in BME calculations reported in Sec. IV B.

The ground state Q values $Q(\rho)$ of the incomplete fusion reaction take care of the observed PE neutron multiplicity $M_{\rm PE}(\rho)$ determined with a moving source fit (cf. Sec. IV A). The numerical values given in Table II were calculated from mass tables[39] for symmetric $(0.4 \le m_N \le 0.6)$ and asymmetric fragmentations in four $\Delta\rho$ windows studied in the subsequent analysis.

B. Linear momentum transfer ρ and fragment mass distributions

The distributions of $v_\parallel$ for all events show a pronounced maximum $\rho_{\rm max}$ corresponding to an LMT of 73% and 77%, respectively (Table III), a shoulder to more peripheral collisions and tails extending beyond 100% LMT; see Fig. 3. These high LMT values are partly due to the broadening of the folding angle distribution by prescission particle evaporation, the uncertainties in the velocity determination, and the approximation inherent to the massive transfer model. Based on the experimentally determined out-of-plane distribution of the coincident fragments which have standard deviations σ_ϕ of 8°–9° (from which 3.5° are due to the detectors $F1$–$F4$ having no spatial resolution) in the four windows below

LMT = 120% indicated in Fig. 3 and increase abruptly to 14.6° (for ^{197}Au) and 17° (for ^{232}Th) for the events beyond 120% LMT, it can be concluded that only values of at most 120% are compatible with a binary process. This point of view will be pursued here to extract an estimate of intermediate mass fragmentations.

Figure 4 shows the distribution of the normalized mass m_N and the LMT for those events with symmetric detection angles $\theta_1=\theta_2=\theta$ within $\Delta\theta=6°$ intervals corresponding to the eight positions of the detectors $F1$–$F4$. The centroids of the LMT distributions shift in accordance with Eqs. (1) and (3) for decreasing θ to higher values; their widths remain roughly constant for $\theta > 57°$. For smaller angles they broaden substantially, because fragmentations extend for a given LMT to smaller folding angles the more asymmetric they are. The main point, however, is that for $\theta < 51°$ (for $^{197}\mathrm{Au}+{}^{32}\mathrm{S}$) and $\theta < 55°$ (for $^{232}\mathrm{Th}+{}^{32}\mathrm{S}$) symmetric fragmentation should kinematically be no more detectable based on TKE systematics.[42] Even a 30% lower TKE shifts these limits only by 5°. Indeed Fig. 4 does show that in this angular range the mass asymmetric fragmentation starts to dominate. There is, however, still a sizable fraction of "symmetric" yield. Selecting the events with the constraint LMT $\geq 120\%$ reveals that these symmetric fragmentations are strongly correlated with these unphysical LMT values. We conclude that these events are actually of nonbinary nature with at least one unobserved intermediate mass fragment; Eqs. (1) and (2) are, however, blind to nonbinary events.

A similar effect can be observed in the fragment mass distributions calculated from Eq. (2) by mans of Eq. (4). For this purpose the evaporated mass m_{evap} was determined with a statistical model calculation. We applied the code JULIAN, whose basic assumptions and input have been described recently.[19] We started the deexcitation by particle evaporation without fission competition at the initial excitation $E^*_{CN}(\rho)$ given in Table II and an angular momentum $I = 80\hbar$. Deexcitation was followed until the experimentally observed prescission neutron multiplicity M_{pre} (cf. Sec. IV C) was reached; the calculation therefore supplemented M_{pre} by the yield of charged particle evaporation. The values calculated this way for m'_{CN} vary between 195 u (Th: 230) for $\rho = 0.35$ and 185 u (Th: 220) for $\rho = 0.97$. Employing these values for m'_{CN} in Eq. (2) yields the fragment mass distributions shown in Fig. 5 for different LMT windows together with the mass distribution obtained from both, fragment velocity and energy measured with the coincident detector $F1$–$F4$. For LMT < 120% reasonable agreement can be stated; the excess of high mass events is an artifact of the energy loss in the target the solid state detector data were not corrected for (in this case). However, for LMT > 120% the one-arm experiment yields substantially lower masses that can be associated with the occurrence of more than two fragments, whereas the two-arm experiment misinterprets the measured velocities under the assumption of a binary fragmentation with inherent normalization to a total mass m'_{CN}.

Klotz-Engmann *et al.*[43] succeeded in using the relative

TABLE II. LMT windows $\Delta\rho$ with centroids $\bar{\rho}$ applied in the analysis of the reactions $^{32}\mathrm{S}+{}^{197}\mathrm{Au}$, $^{32}\mathrm{S}+{}^{232}\mathrm{Th}$. For each window are given the fragmentation into PE nucleons, spectator and CN following participant absorption, the fissility x_{CN} of the CN and the quantities E_{trans}, Q, and E^*_{CN} associated with the incomplete fusion; see Eqs. (5) and (6). The last two columns give the total numbers of observed events for symmetric and asymmetric fission, respectively.

Reaction	LMT window $\Delta\rho$	Centroid $\bar{\rho}$	$E_{\mathrm{trans}}(\bar{\rho})$ (MeV)	Fragmentation	Fissility (Ref. 40) x_{CN}	$Q(\bar{\rho})$ (Ref. 39) (MeV)	$E^*_{CN}(\bar{\rho})$ (MeV)	N_{sym}	N_{asym}
$^{32}\mathrm{S}+{}^{197}\mathrm{Au}$	≤ 0.47	0.35	271	$^{208}_{84}\mathrm{Po}+{}^{18}\mathrm{Ne}+2n+p$	0.71	−70	201	227 150	188 483
	0.47–0.63	0.60	418	$^{215}_{88}\mathrm{Ra}+{}^{10}\mathrm{C}+3n+p$	0.75	−107	311	250 963	369 516
	0.63–0.86	0.74	540	$^{221}_{91}\mathrm{Pa}+\alpha+2n+2p$	0.78	−109	431	467 176	594 989
	0.86–1.20	0.97	683	$^{227}_{95}\mathrm{Am}+2n$	0.82	−115	568	180 081	218 601
$^{32}\mathrm{S}+{}^{232}\mathrm{Th}$	≤ 0.47	0.35	269	$^{243}_{96}\mathrm{Cm}+{}^{17}_{9}\mathrm{F}+p+3n$	0.81	−83	186	184 896	238 184
	0.47–0.64	0.57	431	$^{250}_{99}\mathrm{Es}+{}^{9}_{6}\mathrm{C}+p+4n$	0.83	−133	298	194 217	305 006
	0.64–0.87	0.76	561	$^{256}_{103}\mathrm{Lr}+\alpha+p+3n$	0.87	−117	444	373 614	552 329
	0.87–1.20	0.98	705	$^{261}_{106}\mathrm{X}+3n$	0.90	−124	581	236 545	291 368
	≥ 1.20	1.51						44 765	56 690

TABLE III. Most probable fractional LMT before ($\rho_{\max}$) and after [$\rho_{\max}^{\text{sym}}(\eta),\rho_{\max}^{\text{asym}}(\eta)$] efficiency correction; MF gives the amount of events observed with an apparent LMT > 120%, $\sigma_{\text{CF}}^{(1)}$ is the complete-fusion fission cross section, and $l_{\text{FLMT}}(\sigma_{\text{CF}}^{(1)})$ the associated cutoff angular momentum. l_{crit} is obtained from a one-dimensional potential, and l_{FRM} from a finite-range liquid-drop model calculation (Ref. 45).

Reaction	$\rho_{\max}$	$\rho_{\max}^{\text{sym}}(\eta)$	$\rho_{\max}^{\text{asym}}(\eta)$	MF (%)	$\sigma_{\text{CF}}^{(1)}$ (mb)	$l_{\text{FLMT}}(\sigma_{\text{CF}}^{(1)})$ ($\hbar$)	l_{crit} ($\hbar$)	l_{FRM} ($\hbar$)
^{32}S+^{197}Au	0.73	0.71	0.65	2.3	379±120	106±17	96	≈60
^{32}S+^{232}Th	0.77	0.75	0.65	7.8	332±100	100±15	96	≈45

velocity v_{ff} of the fragments from $\alpha+{}^{197}$Au to discriminate binary from multiple fragmentations with v_{ff}^{s} for the TKE of symmetric fragmentation:[42] however, for the reactions under study the binary fragmentations extend to higher asymmetry and are characterized by values v_{ff} considerably higher than v_{ff}^{s}. The same observation is reported for 30 MeV/u ^{58}Ni on ^{232}Th;[18] therefore v_{ff} does not provide us with a reliable separation tool, cf. Fig. 6.

Instead we decided to characterize the amount of multiple fragmentations by the fraction of events observed with LMT > 120%. They comprise 1.7% (4.9%) of all observed ^{32}S+^{197}Au (^{32}S+^{232}Th) events; it was mentioned before that the out-of-plane distributions are much broader for LMT > 120% than below. If this difference in detector efficiency is corrected for, the fractions 2.3% and 7.8% are obtained. These numbers indicate that we observe with our planar detector geometry with 26.2 MeV/u ^{32}S projectiles and $E_{CN}^{*}\approx 600$ MeV for full momentum transfer the onset of nonbinary fragmentations in qualitative agreement with Refs. 37 and 43 and the expectation[22] of up to 20% under these conditions for a detector system with almost 4π sensitivity. The amounts would be about 50% higher if the threshold were set to LMT ≥ 110%, a value that seems to be a lower limit in view of the uncertainties stated in Sec. II.

For a quantitative description of the LMT distribution Fig. 3 is inadequate, because it is affected by the kinematic detection efficiency η of our setup for binary fragmentations. In order to correct for it, a calculation was performed to determine the fraction $\eta(\rho,m_N)$ of detected events as a function of both LMT and mass split; it was based on the actual detector geometry, the assumption of binary fragmentation with rotational symmetry around the beam axis, a $1/\sin\theta_{\text{c.m.}}$ angular distribution, and TKE values following the generalized[19] Viola systematics. The distortion of the coplanarity due to particle evaporation was neglected. The efficiency correction $\eta^{-1}(\rho,m_N)$ was applied eventwise.

Figure 7 shows the resulting contour plot of normalized mass m_N versus folding angle, and its projection as folding angle distribution with the absolute cross sections deduced from the Rutherford monitor count rates; cf. Fig. 1. The lines in the upper part connecting the *loci* of the LMT value indicated for the extreme assumptions of constant and of scaled[19] TKE reveal that the folding angle varies considerably as a function of fragmentation. Therefore the projections in the lower part also show the contributions of symmetric ($0.4\leq m_N\leq 0.6$) and asymmetric fragmentations. Considering the dependence

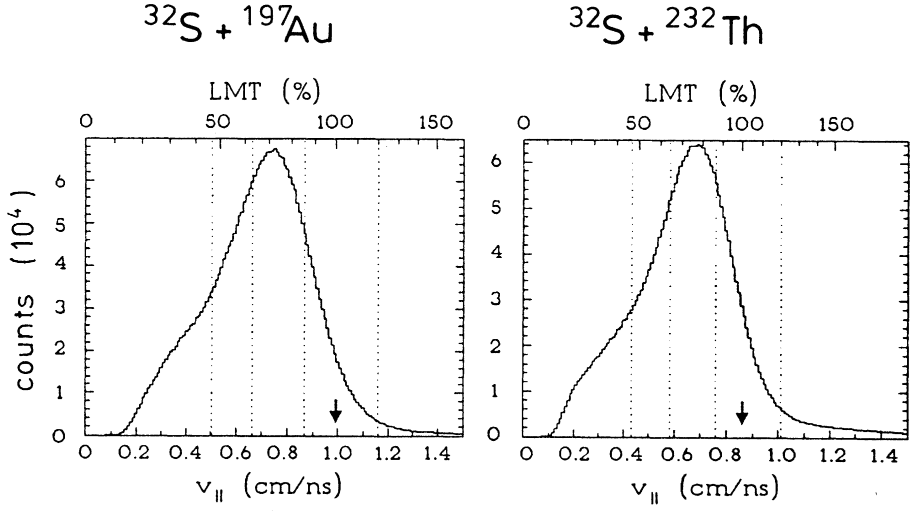

FIG. 3. Distribution of the velocity component $v_{\parallel}$ (recoil velocity) for all detected fragmentations from ^{32}S+^{197}Au,^{232}Th. The arrows indicate the values for complete fusion. The LMT scale results from Eq. (3). The vertical lines separate the LMT windows applied for data analysis.

$\theta_{\text{fold}}(\text{LMT},m_N)$ visible in the upper part of Fig. 7, one can read from the lower part, that the most probable LMT values for violent collisions are significantly higher for the symmetric fragmentations, $\rho_{\max}^{\text{sym}}(\eta)$, than for the asymmetric ones, $\rho_{\max}^{\text{asym}}(\eta)$, which implies that they originate from the more central collisions. The numerical values are listed in Table III.

The second peak close to 160° represents peripheral collisions with considerably lower LMT.[18] This component is much more pronounced in the reaction with ^{232}Th than in the one with ^{197}Au indicating that the more fissile system $^{32}\text{S}+^{232}\text{Th}$ has not only lower barrier heights B_f $(l=0)$,[45] but also lower angular momentum values l_{FRM} for which the fission barrier in the liquid-drop model vanishes (Table III). Therefore the fission yield is in peripheral collisions increased over that from $^{32}\text{S}+^{197}\text{Au}$, whereas for $^{32}\text{S}+^{197}\text{Au}$ the violent events with higher LMT and E^* are more abundant.[37] According to Fig. 7 this filter is more effective for asymmetric fission than for symmetric fragmentations.

The most probable LMT in the central collisions including the efficiency correction is with 72% and 78% close to the value $\rho_{\max}$ read from the maximum value in Fig. 3 (cf. Table III). These values correspond to a transferred momentum of 168±5 MeV/c per projectile nucleon and are in line[46] with the LMT saturation observed for projectiles with $\epsilon=20$–40 MeV/u, e.g., for $^{58}\text{Ni}+^{232}\text{Th}$,[18] $^{14}\text{N}+^{238}\text{U}$,[17] and $^{20}\text{Ne}+^{197}\text{Au},^{209}\text{Bi}$,[20] and for $^{40}\text{Ar}+^{232}\text{Th}$ in this[41] as well as the extended energy range $\epsilon\le 77$ MeV/u.[21]

In our fissility range the fusion-fission cross section with full LMT can be identified with the complete fusion cross section σ_{CF}, because evaporation residue formation is highly improbable.[46,47] The fission events in the LMT window $0.9\le\rho\le 1.1$ show an angular distribution that is compatible with a $1/\sin\theta_{\text{c.m.}}$ dependence. The integration can be performed with the normalization constant derived from the Rutherford monitors under $\theta_{\text{lab}}=8°$ and yields the values $\sigma_{\text{CF}}^{(1)}$ listed in Table III. The quoted uncertainty estimate results from a variation of the window

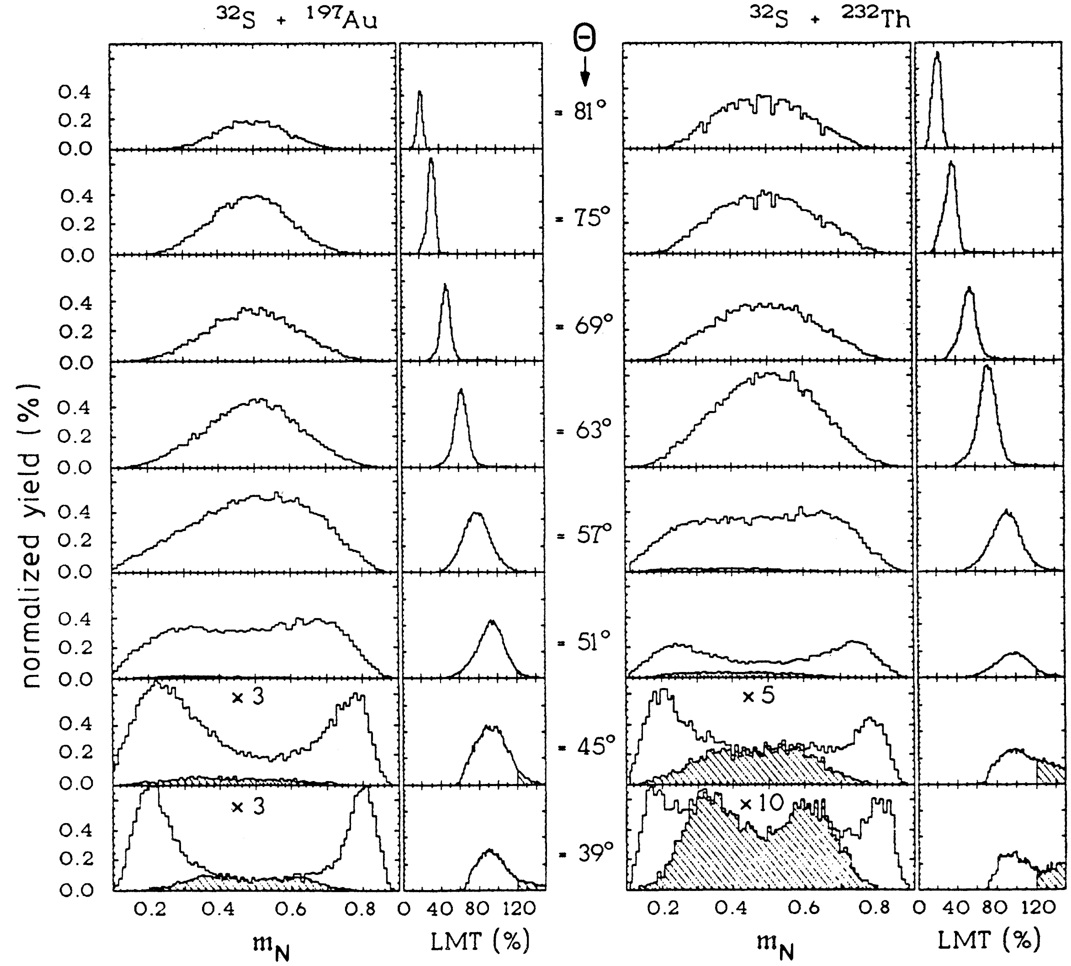

FIG. 4. Yield (normalized to 100%) of relative fragment masses m_N for the symmetric detector angles $\theta_{\text{MWC}}=\theta_F=\theta$ indicated. The respective LMT distributions are shown, too. The hatched areas cover the contributions of events with more than 120% (calculated) LMT. Some histograms are multiplied by factors shown.

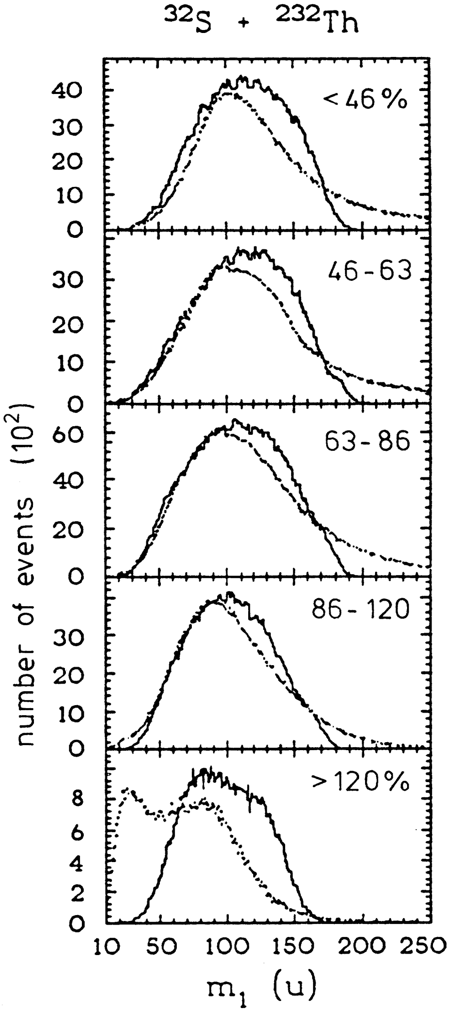

FIG. 5. Mass distributions for fragmentations of ^{32}S+^{232}Th in the indicated LMT bins of Fig. 3 obtained (solid line) from Eq. (2) and (dotted) from energy plus velocity measured with a solid state detector.

by $\Delta\rho = 0.05$.

Following Tubbs *et al.*[47] the folding angle distribution can be unfolded into several contributions of Gaussian shapes with centroids corresponding to 0–7 α particles from the projectile. The widths in ϕ and θ were identified with those measured in the out-of-plane correlation. Such a Gaussian has been fitted around the centroid for symmetric fragmentation after 100% LMT including a modification for LMT values > 100% [cf. Fig. 7(b)]. The resulting cross sections $\sigma_{\mathrm{CF}}^{(2)}$ of 480±190 mb for both reactions represent an upper limit.[30]

Integration over the total LMT distributions shown in Fig. 7(b) gives an estimate of the total cross section σ_{BE} for binary events including those from peripheral collisions with a gradual transition to target plus projectile like fragments or residues plus projectile remnants. It was performed under the assumption of an angular distribution $\sim(\sin\theta_{\mathrm{c.m.}})^{-1}$ and with some correction for the folding angles $\theta_{\mathrm{fold}} > 167°$ and $\theta_{\mathrm{fold}} < 71°$ not accessible here, but in Ref. 48 for ^{40}Ar+^{232}Th at 27.2 MeV/u; the result is $\sigma_{\mathrm{BE}} = 4400$ mb (4100 mb) for ^{32}S+^{197}Au (^{32}S+^{232}Th) with an estimated uncertainty of ±25%.

One can restrict the integration to the central collision peak to extract the fusion-fission cross section. These events show a distribution $\sim(\sin\theta_{\mathrm{c.m.}})^{-1}$ in the angular range accessible with our setup. An uncertainty is introduced by the extrapolation of the central collision peak on the low LMT side. The integration yields a fusion-fission cross section $\sigma_{\mathrm{FF}} = 2100$ mb for ^{32}S+^{197}Au and 1700 mb for ^{32}S+^{232}Th, each with an uncertainty of ±20%.

The values for σ_{FF} can be compared with the total reaction cross sections[49] σ_R of 4200 mb (4330 mb):

$$\sigma_{\mathrm{FF}}/\sigma_R \approx 0.4\text{–}0.5 \ . \tag{7}$$

For ^{32}S projectiles of 26.2 MeV/u on heavy targets the total reaction cross section is therefore to almost 50% leading to central, highly dissipative collisions. In Ref. 44, $\sigma_{\mathrm{FF}} \approx 2300$ mb or a ratio $\sigma_{\mathrm{FF}}/\sigma_R$ of almost 50% was

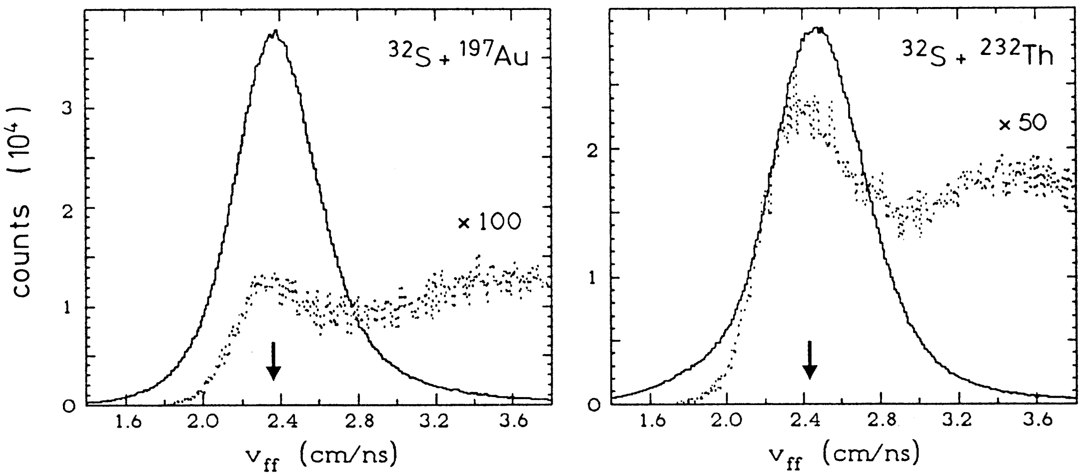

FIG. 6. Distributions of relative velocities v_{ff} of coincident fragments for events with less than (solid histogram) and more than 120% LMT; the latter ones are multiplied by the factors shown. The values resulting from Ref. 42 for symmetric fission are indicated by an arrow.

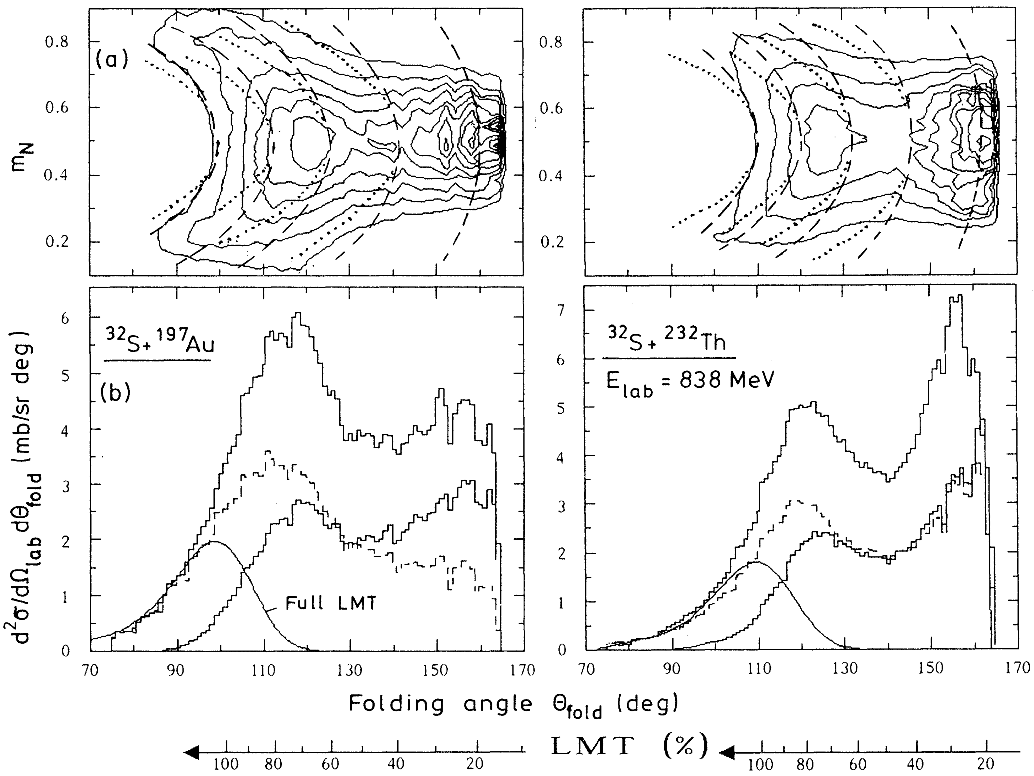

FIG. 7. Top: Contour plot of folding angle versus normalized fragment mass for all events; the yield increases by 10% between adjacent lines. The dashed (dotted) lines connect loci with LMT values of 20%,40%, . . . , 100% based on a constant (Ref. 42) [fragmentation dependent (Ref. 19)] TKE. Bottom: Projection onto the folding angle axis for all events (upper solid line), those with symmetric ($0.4 \le m_N \le 0.6$, lower solid line) and asymmetric fragmentations (dashed). The thin solid line gives the estimated distribution of events with full LMT (including all with more than 100% LMT). The LMT scale refers to symmetric fragmentations.

found for ^{40}Ar on ^{238}U at 27 MeV/u, in close agreement with our result, Eq. (7). However, $\sigma_{\rm CF}^{(1)}/\sigma_R \approx 0.1$, i.e., only about 10% of all inelastic interactions lead to complete fusion.

In a sharp cutoff approximation, $\sigma_{\rm CF}^{(1)}$ can be converted into an angular momentum $l_{\rm FLMT}$ with the meaning that only central collision with $l \le l_{\rm FLMT}$ in the entrance channel leads to complete fusion. The resulting values (cf. Table III) are in agreement with the critical value $l_{\rm crit} = 96\hbar$ of a vanishing potential pocket. Secondly, $l_{\rm FLMT} \approx 100\hbar$ can be converted into a radial distance $\Delta R = l_{\rm FLMT}/p$, where $p = 7090$ MeV/c is the linear momentum of the ^{32}S projectiles. The result $\Delta R = 2.8$ fm is slightly lower than the difference of the equivalent sharp surface radii[49] (3.27 fm for ^{32}S+^{197}Au) and allows the interpretation that the violent collisions with total overlap of projectile and target nucleus do indeed lead to fusion-fission-like events.

The finite-range liquid-drop model[45] (FRM) predicts the saddle point to disappear for values $l_{\rm FRM}$ of about $60\hbar$ ($45\hbar$) for ^{32}S+^{197}Au(^{232}Th). The ratio $(l_{\rm FRM}/l_{\rm FLMT})^2$ may be considered a measure for the fraction of fusion-fission events among all events with full LMT including fission-like processes;[50] it amounts to 31% and 20%, respectively, with the lower value for ^{32}S+^{232}Th reflecting the lower fission barrier in central collisions, $V_B(l=0) \approx 0.3$ MeV, as compared to $V_B(l=0) \approx 2.5$ MeV for ^{32}S+^{197}Au.[45] The corresponding numbers for the composite system following 35% LMT are 3.0 and 10.5 MeV. These differences are responsible for the different shapes of the LMT distributions in Fig. 7(b), too.

IV. FISSION COINCIDENT NEUTRON SPECTROSCOPY

A. Moving source decomposition

The measured double differential neutron multiplicities $M(E_n,\theta_n)$ per fission event reveal a complex dependence on both E_n and θ_n. An example is shown in Fig. 8. For further analysis, the valid triple coincidences were subdivided into 12 subgroups with comparable statistics, namely (a) three classes of fragmentations: $m_N \le 0.4$,0.4–0.6, ≥ 0.6, and (b) four classes of LMT as listed in Table II. In addition, a correlation with TKE was searched for among the symmetric fragmentations establishing three classes out of each LMT group; this discussion is deferred to Sec. IV C 3.

For each subgroup, the multiplicities $M(E_n,\theta_n)$ were considered[51] an incoherent sum of altogether four contributing moving sources, viz.,

$$\frac{d^2M_n(E_n,\theta_n)}{dE_n\,d\Omega(\theta_n)} = \sum_{i=1}^{4} \frac{M_i}{2(\pi T_i)^{3/2}}\cdot E_n^{1/2}\exp\left[-\frac{E_n-2\sqrt{E_n\epsilon_i}\cosh\psi_i+\epsilon_i}{T_i}\right] . \tag{8}$$

Each term i corresponds to a source moving with an energy per nucleon ϵ_i that emits M_i neutrons isotropically in its rest frame with the spectral shape of a Watt distribution.[52] The temperature parameter T_i actually represents an average over the neutron cascade originating from a source with initial temperature $T_{0i}=\frac{12}{11}T_i$.[53] The neutron emission angle ψ_i is measured with respect to the direction of the moving source. The sources are identified with the precompound emission (i=PE), emission after (incomplete) fusion prior to scission (i=pre) and emission from fully accelerated fragments (i=post).

Equation (8) was evaluated by performing a least-squares fit of the right-hand side with the same set of parameters simultaneously to the spectra of all eight neutron detectors $N1$–$N8$. The free parameters were the multiplicities M_i, "temperatures" T_i, and for the PE source also the source velocity, i.e., ϵ_i. For the composite system as well as for the fragments, the experimental values for ϵ_i were averaged over the subgroup of events under consideration and then kept fixed in the fit procedure. The resulting parameter sets are listed in Tables IV and V; the velocities v_{PE} of the PE source are shown in Fig. 9. The uncertainties quoted correspond to an increase of χ^2 by 10% over the minimum value.

The comparison of the fit results for $\theta_n=\pm 39°$ in the representative example (Fig. 8) reveals the focusing effect by fragment sources moving towards the respective neutron detector; but even under these angles the compound source is the dominant one. This is clear evidence for the prescission neutron multiplicity being larger than the postscission ones. Neutron detector $N4$ was the only one positioned out of plane ($\phi=90°$); the fit to $N4$ is of the same quality as to the other spectra and there is again[19] no indication for a deviation from an isotropic emission of the equilibrium sources. The high energy yield beyond $E_n=20$ MeV can only be accounted for by a PE source, whose distribution is highly forward peaked in the laboratory frame due to a velocity comparable to the beam velocity. In this region, however, the statistics require the events to be grouped into broader bins of up to 10 MeV width.

B. The preequilibrium source

The velocities v_{PE} and temperatures T_{PE} displayed in Fig. 9 as a function of the LMT show a striking similarity

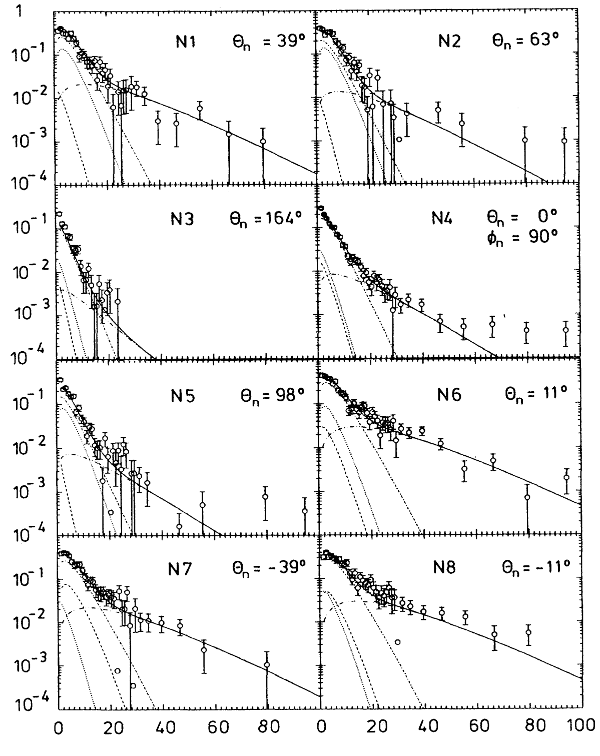

FIG. 8. Experimental (dots) multiplicities $M(E_n,\theta_n)$ for the symmetric fragmentation of ^{32}S+^{197}Au in the highest LMT window $\bar{\rho}=0.97$. The moving source fit is given by its individual contributions from PE (dash-double-dotted line), left (dotted) and right (dashed) fragment, and compound nucleus (dash-dotted) source—as well as their sum (solid line).

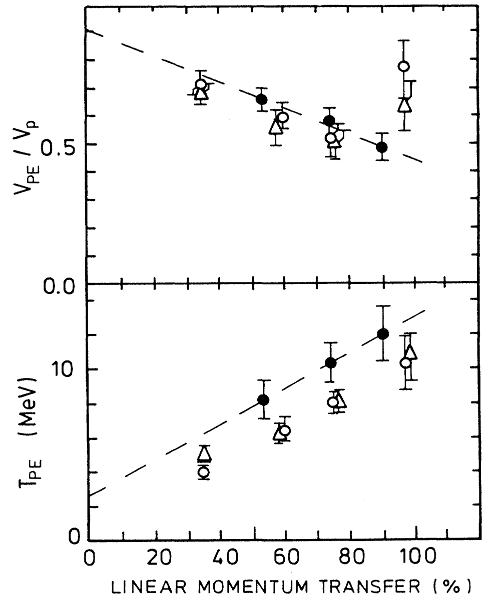

FIG. 9. Temperature T_{PE} and velocity v_{PE} (in units of the projectile velocity v_p) of the PE sources for ^{32}S+^{197}Au (open circles), ^{32}S+^{232}Th (open triangles), and for ^{20}Ne+^{165}Ho (solid circles, Ref. 35); the latter results are connected by a line to guide the eye.

TABLE IV. Preequilibrium, prescission, and postscission neutron multiplicities for symmetric and asymmetric fragmentations and different LMT windows obtained from moving source fits.

Reaction	$\bar{p}$	E^*_{CN} (MeV)	M_{PE}	Symmetric fragmentation M_{pre}	Symmetric fragmentation M_{post}	Asymmetric fragmentation M_{pre}	Asymmetric fragmentation M_{post}
^{32}S+^{197}Au	0.35	201	3.0±0.3	7.7±1.8	7.2±2.0	8.0±1.9	7.3±1.9
	0.60	311	4.4±0.6	10.7±2.5	7.4±2.7	10.2±1.8	7.3±1.8
	0.74	431	4.1±0.5	13.3±1.9	6.7±1.8	11.3±1.7	8.5±1.6
	0.97	568	2.4±0.7	15.9±2.4	6.0±3.2	13.2±1.7	7.3±2.6
^{32}S+^{232}Th	0.35	186	4.3±0.4	11.3±2.3	8.4±2.4	9.6±2.3	9.2±2.8
	0.57	298	5.0±0.8	14.1±2.4	10.3±2.5	13.4±1.3	9.1±1.4
	0.76	444	4.1±0.5	16.9±2.5	8.9±2.5	15.3±1.7	10.2±1.7
	0.98	581	2.8±0.7	19.9±2.5	7.3±3.1	19.0±2.3	7.2±2.8

for both reactions under study. The observable trends are as follows.

(i) The temperature parameter increases linearly with LMT. If a large LMT value according to Eq. (5) is associated with a more central and therefore more violent collision, this finding allows the interpretation of a very fast PE emission that benefits from the *total* amount of excitation energy brought into the reaction system. In addition the decrease of T_{PE} with LMT may indicate that we observe in more peripheral collisions a superposition of sequential and PE emission.[54] This view is supported by the fact that extrapolation to LMT ≈ 0 yields a temperature T_{PE} of 1–2 MeV, i.e., in the range of those for the fragments (Table V). The same trend was observed for PE emission preceding evaporation residue (ER) formation in the reaction of 30 MeV/u projectiles ^{20}Ne with ^{165}Ho,[35] cf. Fig. 9. However, there the absolute values for T_{PE} are systematically higher due to the higher values of ϵ or $(E-V_{\mathrm{Coul}})/A$,[55] and secondly, because ER formation goes together with more central collisions than in fusion-fission events.

(ii) The velocity parameter decreases with increasing LMT and for the most probable LMT value (75%) velocities $v_{\mathrm{PE}}/v \approx 0.5$ result. The latter value has been observed repeatedly and in particular for ^{20}Ne+^{165}Ho. However, there is a striking difference visible for 100% LMT. Whereas for ^{20}Ne+^{165}Ho, the velocity v_{PE} continues to decrease, the fusion-fission data from ^{32}S+^{197}Au,^{232}Th show a clear upward trend. In this LMT window the PE source tends to approach $v_{\mathrm{PE}} \approx v$ which is indicative of a more direct neutron emission in collisions yielding intermediate mass fragments. This result is in line with the observed onset of multifragmentation (Sec. III B).

The PE nucleon emission has been explored successfully with the Boltzmann master equation (BME) model that follows the relaxation of an excited nucleus via internal nucleon-nucleon collisions in time increments $\Delta t \approx 2\times 10^{-23}$ s. An energy space is considered which is initially filled with nucleons up to the Fermi energy. The excitation energy is introduced with a time dependent injection of projectile excitons into the coalescing system. Blann[10] applies a source term related to the n_0 exciton state density which is injected with the projectile velocity at the top of the Coulomb barrier and with $n_0 \approx A_{\mathrm{proj}}$. The model has proved its predictive power for the reactions ^{20}Ne+^{165}Ho (Ref. 56) and $\epsilon \leq 20$ MeV/u as well as for ^{14}N, ^{40}Ar, and ^{58}Ni induced reactions[18] with $\epsilon \leq 60$ MeV/u and associates the saturation of LMT values discussed in Sec. III *B* with the amount of preequilibrium nucleon emission. This means that the central collision peak in the folding angle distribution does indeed result from the interaction of the entire projectile with the target.[17,18]

We have performed a BME calculation[10] for ^{32}S+^{197}Au,^{232}Th; the PE phase was restricted to the first 30 time increments corresponding to an equilibration time of 6×10^{-22} s. The results are compared in Table VI

TABLE V. Source temperatures T (in MeV) obtained from moving source fits for the four sources considered separately for events with symmetric and asymmetric fragmentation. $T_{\mathrm{eq}}(E^*_{CN})$ is calculated from Eq. (9) and T_{sm} from the average kinetic energies $\bar{E}_n$ of neutrons from a statistical model calculation with $k=10$ MeV (8 MeV).

					Asymmetric fragmentation				
	E^*_{CN}/A_{CN}		Symmetric fragm.			T_{post}		Calculations	
Reaction	(MeV/u)	T_{PE}	T_{pre}	T_{post}	T_{pre}	Heavy fr.	Light fr.	$T_{\mathrm{eq}}(E^*_{CN})$	T_{sm}
^{32}S+^{197}Au	0.97	3.9±0.3	2.4±0.3	1.7±0.4	2.7±0.3	1.9±0.4	1.5±0.5	3.0(2.7)	3.2(3.0)
	1.45	6.3±0.5	3.3±0.4	1.6±0.4	3.1±0.3	1.7±0.4	1.7±0.5	3.7(3.3)	3.7(3.5)
	1.95	8.0±0.5	3.4±0.3	1.8±0.3	3.5±0.3	2.0±0.3	2.1±0.3	4.3(3.9)	4.2(4.0)
	2.50	10.2±1.6	3.7±0.3	2.0±0.4	3.2±0.3	2.2±0.4	3.5±0.8	4.9(4.4)	4.5(4.3)
^{32}S+^{232}Th	0.71	4.9±0.4	2.8±0.3	1.4±0.4	2.9±0.3	1.6±0.6	1.4±0.4	2.7(2.4)	2.4(2.2)
	1.19	6.1±0.5	3.3±0.4	1.7±0.4	3.0±0.3	2.6±0.3	1.7±0.4	3.4(3.0)	3.3(3.1)
	1.73	8.1±0.6	3.3±0.3	1.8±0.3	3.5±0.2	1.8±0.3	1.9±0.3	4.1(3.7)	3.9(3.7)
	2.22	10.6±1.4	3.5±0.3	1.9±0.5	3.2±0.3	2.1±0.5	3.0±0.5	4.7(4.2)	4.5(4.2)

TABLE VI. Comparison of experimental data with results of a BME calculation.

	^{32}S+^{197}Au		^{32}S+^{232}Th	
	BME	Exp.	BME	Exp.
$\bar{\rho}$	0.78	0.74	0.79	0.76
$M_{\mathrm{PE}}^{(n)}$	4.5	4.1	5.2	4.1
$\bar{E}_n$ (MeV)	14.3	12.0$^{\mathrm{a}}$	13.9	12.2$^{\mathrm{a}}$
$M_{\mathrm{PE}}^{(p)}$	2.2		1.5	
$\bar{E}_p$ (MeV)	28.2		31.3	
E_{CN}^* (MeV)	442	431$^{\mathrm{b}}$	462	444$^{\mathrm{b}}$

[a] Calculated as $\bar{E}_n = \frac{3}{2} T_{\mathrm{PE}}$.

[b] From Eq. (5).

with the experimental ones for symmetric fragmentation in the LMT window containing the central collision peak. Keeping in mind the uncertainties of the model calculation due to alternatives for the injection term,[11] the definition of the equilibration time and the inability to differ between bound and unbound nucleons in PE emission which lead to $\Delta\rho \approx 1\text{–}2\,\%$, $\Delta E^* \approx 15\text{–}20$ MeV and $\Delta M_n \approx 1$, the agreement must be considered excellent. In particular the excitation energy E_{CN}^* confirms the value calculated from Eq. (5) that is based on a different approach, namely the massive transfer model.

Finally, it must be pointed out that the parameters T_{PE}, v_{PE}, and M_{PE} deduced depend on the assumed characteristics of a PE source, that it emits isotropically and moves with constant velocity. Indications for preferential PE neutron emission in the reaction plane[54,58] and in forward directions[59,60] have been recently reported. We have implemented the concept of Ref. 59 into the emission characteristics of the PE source. The resulting PE parameters indicate anisotropic sources that are *slower* and *hotter*, i.e., the anisotropy in the laboratory frame is equally well taken care of by an anisotropy in the rest frame or by an enhanced source velocity. The spectral shapes, however, and the multiplicities M_{PE} are practically identical. In contrast, the second assumption can lead to substantial discrepancies as was shown in Ref. 61 with a comparison to a BME calculation. The application of this model to the two reactions under study did, however, yield good agreement in the multiplicities M_{PE} (cf. Table IV). All further interpretations in this paper are therefore based on a PE source described with these two assumptions.

C. The equilibrium sources

1. Multiplicities

The survey of multiplicities in Fig. 10 as a function of the linear momentum transferred reveals some clear trends. The prescission multiplicities M_{pre} of both symmetric and asymmetric fragmentations increase almost linearly with LMT and therefore, according to Eq. (6), also with the initial excitation energy E_{CN}^*. The gradient $\Delta E_{CN}^*/\Delta M_{\mathrm{pre}}$ of 46±12 MeV is in excellent agreement with the average value 50 MeV derived from a broad range of data.[50] Only for the asymmetric fragmentation in ^{32}S+^{197}Au this slope is about 25 MeV higher; this may be a consequence of the filter effect mentioned (cf. Fig. 7) insofar as for these asymmetric fragmentations the peripheral collisions are suppressed in particular in the lower LMT windows and the increase of M_{pre} with E_{CN}^* flattens.

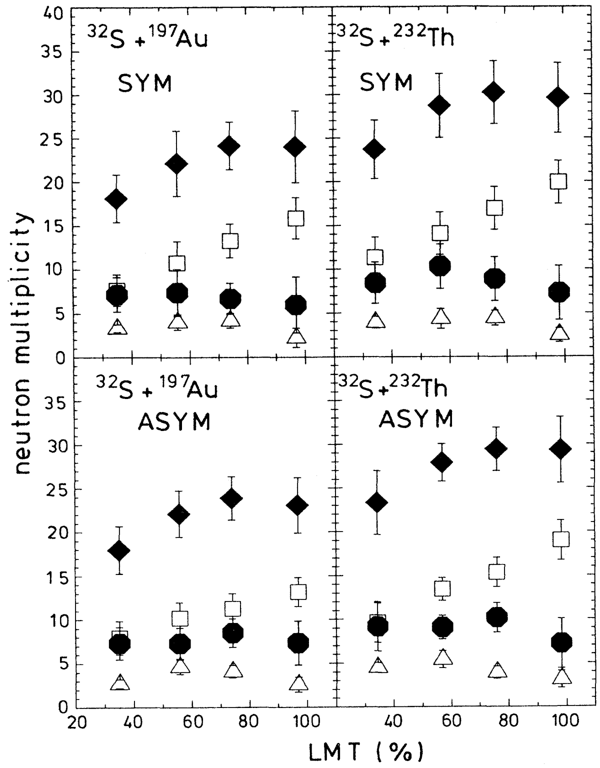

FIG. 10. Neutron multiplicities of the PE (△) and the prescission (□) source, the sum of the two postscission sources (○), and the total (◇) as a function of average LMT values for symmetric and asymmetric fragmentations.

A second distinct feature is the systematic difference in total multiplicities M_{tot} of about 6 neutrons between the two reactions ^{32}S+^{197}Au and ^{232}Th under comparable conditions. This is not an effect of an incorrect detection efficiency, because M_{tot} has been confirmed twofold in an independent measurement combining a neutron TOF with a scintillator tank measurement.[62] It rather reflects that, besides the influence of the effective Q value for fission, at a given initial excitation E_{CN}^* neutron emission from the lighter system ^{32}S+^{197}Au compete less favorably with charged particle evaporation, whereas differences in the neutron separation energies play only a minor role; a quantitative explanation along this line will be given in Sec. V A.

The postscission multiplicities M_{post} do not benefit from the increase of E_{CN}^* with LMT but remain essentially constant. This indicates that only a limited excitation energy remains available to the fragments at the end of the prescission cascade. This phenomenon is not dependent on the initial angular momentum distribution;[63] it has been observed for ^{32}S+^{144,154}Sm, too,[6] and was there attributed to the dynamical time scale of fission. This point will be addressed in Sec. V with the neutron clock. At the moment we note only that the values for $M_{\rm post}$ are systematically higher for asymmetric than for symmetric fragmentations which indicates the former one to be the faster or more direct process due to, e.g., the smaller extent of rearrangement of nuclear matter and mass flow leading from the entrance to the exit channel. The decrease of $M_{\rm post}$ in the highest LMT window in particular for the asymmetric fragmentation of ^{32}S+^{232}Th may be not real, but an artifact of the multifragmentation processes with simulated LMT values below 120%; cf. Sec. III B.

In addition we observe that $M_{\rm post}$ is 1–2 neutrons higher for ^{32}S+^{232}Th than for ^{32}S+^{197}Au. This is not the trivial outcome of differences between the average neutron separation energies[39] from the respective fragments after, e.g., symmetric fragmentation, but is in line with the general trend of $M_{\rm post}$ as a function of the fissility of the composite system shown in Fig. 11. Our results are those for symmetric fission in the third LMT window ($\bar{\rho}=0.75$) and are scaled down to a lower initial excitation by reduction of $M_{\rm post}$ with $\Delta M_{\rm post}/\Delta E_{CN}^*=200$ MeV^{-1}.[50] The smooth rise of $M_{\rm post}$ with fissility is supposed to be associated[1] with the increase of the effective fission Q value $Q_{\rm eff}$ (i.e., mass difference minus TKE). The excess of postfission yield beyond the expectation for fragments of constant temperature $T=1.5$ MeV visible for $x \geq 0.8$ has been explained[64] by the average number of neutrons emitted in spontaneous fission or thermal neutron induced fission extrapolated to zero excitation energy.

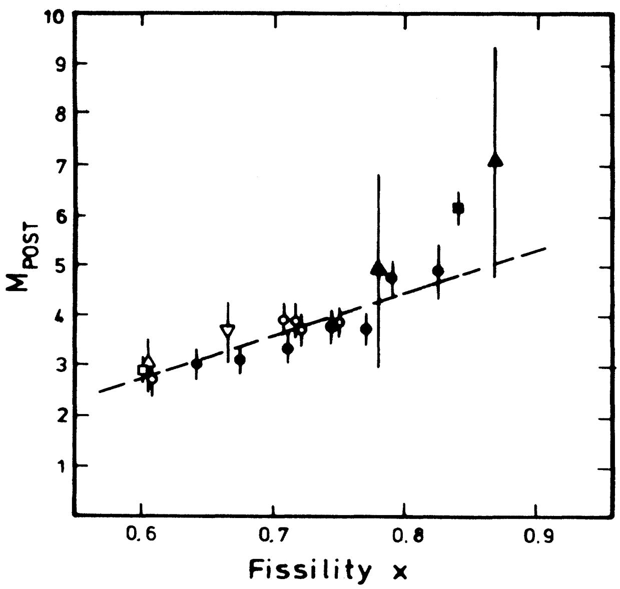

FIG. 11. Postscission multiplicities for fusion-fission reactions as a function of the fissility x of composite systems with initial excitation energies $E_{CN}^* < 150$ MeV. Solid triangles: this work, most probable LMT window; all other reactions are adapted from the compilation in Ref. 1. The line gives the expected values for fragments with $T=1.5$ MeV.

Therefore we conclude for ^{32}S+^{197}Au,^{232}Th from Fig. 11, that the fragment excitation energy E_{SC}^* at scission provides four (for ^{32}S+^{197}Au) to five (for ^{32}S+^{232}Th) postscission neutrons following symmetric fragmentation. Adapting average kinetic energies $\bar{E}_n=\frac{3}{2}\ T_{\rm post}$ with values $T_{\rm post}$ from Table V, average separation energies $S_n \approx 7.6$ MeV,[39] and a correction of $E_\gamma \approx S_n$ for γ deexcitation,[7] we find $E_{SC}^*=51$–59 MeV. For asymmetric fragmentations, the values $M_{\rm post}$ are at most one unit higher. We conclude that the system undergoing scission is left with an excitation energy of 50–60 MeV in complete agreement with the result for ^{32}S+^{144,154}Sm.[6]

The separation of prescission and postscission neutrons rests heavily on the assumption of sources moving with constant velocity. Postscission neutrons emitted during the acceleration phase of the fragments will therefore in part be erroneously attributed to the prescission source. An estimate of this effect has been given elsewhere;[7,19,65] it is minute, because the acceleration time is small ($<10^{-20}$ s) compared to the time necessary to emit a neutron from a fragment excited to 50 MeV or less. For our system at most 0.3 fragment neutrons could be misinterpreted this way. This number would change none of the conclusions drawn in this paper.

2. *Temperature parameters*

The equilibrium temperatures obtained as a function of LMT and fragmentation class are listed in Table V. The prescission temperatures are within the uncertainty limits not dependent on the subsequent type of fragmentation and have the same absolute values for both reaction systems with similar excitation energies per nucleon $\epsilon_{CN}^*=E_{CN}^*/A_{CN}$. They increase with E_{CN}^*, but less pronounced than would be anticipated from the Fermi gas relation

$$aT_{\rm eq}^2(E_{CN}^*)=E_{CN}^*-S_n-2T_{\rm eq}(E_{CN}^*)\ , \qquad (9)$$

where $a=A_{CN}/k$ is the level density parameter and $k \approx 8$ MeV.[21,36,66] The origin is a qualitative difference; the values $T_{\rm pre}$ are *apparent* temperatures, i.e., weighted over the whole cascade of sequential particle evaporation, whereas $T_{\rm eq}$ is the *initial* temperature, i.e., that of the first daughter nucleus. According to Ref. 53 this difference is taken care of in a pure neutron cascade with a factor $\frac{12}{11}$; Gonin *et al.*,[66] however, found that the discrepancy between initial and apparent temperature increases with $E_{\rm CN}^*$ and is particularly high in the neutron exit channel due to the enhanced charged particle emission. This is why insertion of the temperatures $\frac{12}{11}\ T_{\rm pre}$ for $T_{\rm eq}(E_{CN}^*)$ in Eq. (9) yields values for k decreasing with increasing ϵ_{CN}^*, whereas the opposite trend is reported[66] for the initial temperatures and $\epsilon_{CN}^* \geq 2$ MeV. Nevertheless, a general consistency between the excitation energies E_{CN}^* derived with Eq. (5) and the observed temperatures $\frac{12}{11}\ T_{\rm pre}$ can be stated for $k \approx 8$ MeV.

The postscission temperatures $T_{\rm post}$ in contrast show only a faint dependence on E_{CN}^* for symmetric fragmentations, which is obscured in the case of asymmetric fragmentations by a broader scattering of the best fit values—most probably due to the more heterogeneous reaction mechanisms. The most interesting fact is the absolute value of 1.75±0.25 MeV, which is about a factor of 2 higher than for systems with comparable fissility initially excited to $E^*_{CN} \approx 30$ MeV.[7] It converts with Eq. (9) and $k=8$ MeV into an excitation energy $E^*_{F1}+E^*_{F2}$ of the fragments of 83±20 MeV (for ^{232}Th: 97±25 MeV). The values are in good agreement with $E^*_{F1}+E^*_{F2}$ being calculated from the average values $M_{\rm post}$ of Table IV as $M_{\rm post}(1.5T_{\rm post}+S_n)+E_\gamma$; they seem to be higher than the 50–60 MeV of excitation energy E^*_{SC} available at scission, cf. Sec. IV C 1. One possible explanation may be that the fragment excitation energy $E^*_{F1}+E^*_{F2}$ is composed of an intrinsic part E^*_{SC} reflecting the statistical equilibrium up to the scission point, and a contribution resulting from the deformation of the nascent fragments.[7]

3. Dependence of $M_{\rm pre}$ on TKE

Recently, an increase of $M_{\rm pre}$ with TKE was observed in the reaction systems ^{36}Ar+^{169}Tm at $E_{\rm lab}=250$ MeV,[19] and ^{40}Ar+^{165}Ho,^{238}U at $E_{\rm lab}=249$ MeV.[1] Such a correlation would supplement the understanding of fission time scales, because variations in TKE can be associated with different elongations of the scission configurations. Meanwhile, however, these particular correlations have been explained[57] by recoil effects of postscission neutrons which sensitively influence the fragment velocities. It seemed nevertheless worth looking for such a correlation in the present data.

Therefore a fit with four moving sources has been performed with our data for symmetric $(0.4 \le m_N \le 0.6)$ fission, which were for this purpose not only grouped according to their LMT as before, but in addition into the three disjunctive TKE classes with centroids of 120, 149, and 175 MeV (for ^{32}S+^{232}Th: 125, 156, and 190 MeV). The resulting multiplicities are characterized by larger substantial uncertainties due to the additional selection of TKE.

The prescission multiplicities are within the uncertainties compatible with a constant value independent of TKE, which is identical with the value obtained without subdivision into TKE classes; cf. Table IV. This result will not qualitatively change with the inclusion of the recoil corrections.[57] The reason is the following. Due to the high excitations $E^*_{CN} \ge 180$ MeV and their broad distributions in the respective LMT windows, the prescission multiplicities are the dominant ones and anticipated variations of $\Delta M_{\rm pre} \approx 1$–2 units are hard—if at all—to detect, if the uncertainties in the fit values are inherently of the same size.

V. SCISSION TIME SCALES

A. the statistical model

Conceptionally, the neutron clock is set to zero once the equilibration phase of duration $\tau_{\rm PE}$ has reached the equilibrium distribution of excitation E^*_{CN}, spin I, and a shape which is assumed to be that of the ground state minimum. In a statistical model description, the time elapsing until the first decay takes place is given by

$$\tau_{sm,1}=\hbar/\Gamma_{\rm tot} \tag{10}$$

where $\Gamma_{\rm tot}$ is the sum of all partial widths Γ_i competing. The neutron decay width herein is calculated with transmission coefficients T_l as

$$\Gamma_n(E^*,I)=\frac{(2S_n+1)}{2\pi\rho(E^*,I)}\sum_{l=0}^{\infty}\sum_{J=I-l}^{I+l}\int_0^{E^*-S_n}\rho(E^*-S_n-\epsilon_n,J)T_l(\epsilon_n)d\epsilon_n \ . \tag{11}$$

Similar expressions hold for charged particle emission with a total decay width $\Gamma_{\rm ch}(E^*,I)$; for the level densities, the expression

$$\rho(E^*,J)\sim\frac{2J+1}{(E^*-E_{\rm rot})^2}\exp[2\sqrt{a_n(E^*-E_{\rm rot})}] \tag{12}$$

will be used with the level-density parameter a_n and the rotational energy $E_{\rm rot}$. Excitation energies E^*_{CN} of more than 100 MeV lead in heavy nuclei[25,50] to emission times $\tau_n < 10^{-20}$ s; therefore prescission neutron multiplicities $M_{\rm pre}$ can be converted into scission time scales via

$$\tau^{(n)}_{sm}=\sum_{i=1}^{M_{\rm pre}}\tau^{(n)}_{sm,i}=\sum_{i=1}^{M_{\rm pre}}\frac{\hbar}{\Gamma_{n,i}}\left[\frac{\Gamma_{n,i}}{\Gamma_{n,i}+\Gamma_{{\rm ch},i}}\right] \ . \tag{13}$$

This expression needs some discussion concerning its limitations. For sufficiently high values E^*_{CN}, the decay time $\tau_{s,m1}$ may drop below the dissipation time $\tau_{\rm PE}$ which is in the order of 5×10^{-22} s.[10] This will happen if $\sqrt{E^*_{CN}/a_n}$ is in the order of 5 MeV,[12] which is beyond the range of the present experiment. Also, at these high excitations the parameters entering into Eq. (11)—in particular the level-density parameters, but to a lesser extent their ratios—are not accurately enough known or energy dependent.[66] However, the significant contributions to Eq. (13) come from the last few neutrons[1,2] where the emitting system has essentially cooled down to $E^* \le 100$ MeV and a parameters are less prone to uncertainties.

Finally it must be stressed that Eqs. (11) and (12) require a value of E^* which is certainly overestimated by considering the frozen equilibrium shape; instead, the system develops towards the scission point with consequences for E^* as well as a. The implications hereof are discussed in Refs. 2 and 9 and shall not be repeated here.

The subsequent calculations with the code JULIAN were performed under the assumption of particle evaporation only from *spherical* reaction systems with the initial excitation energies E^*_{CN}(LMT) from Table II and a fixed initial value of $I=80\hbar$. This value was applied in

Ref. 6 to the reaction $^{32}S+^{144,154}Sm$, too; it is about $10\hbar$ larger than the mean value resulting from an approximation of the entrance channel distribution with a sharp cutoff at l_{FLMT}, cf. Table III. A ratio of the level-density parameters for particle (n,p,d,α) emission and fission $a_n/a_f=1$ was applied. Transmission coefficients T_l for ejectile evaporation were calculated with the optical model and standard parameter sets; the spin dependent fission barrier heights were taken from the finite-range liquid-drop model.[45] More details are given in Ref. 19. The onset of the statistical fission competition was delayed by a time interval Δ adjusted in length such that the experimental observed prescission multiplicities M_{pre} were reproduced.

The deexcitation was then followed further including (symmetric) fission as additional decay channel. Finally the excitation energy $E_{F1}^*+E_{F2}^*$ stored in the fragments was exhausted in particle (mostly neutron) emission and γ deexcitation. The calculations were performed for $a=A/k$ with $k=8$, 10, and 13 MeV. In all cases fission turned out to dominate over the competing channels leading to evaporation residue formation; therefore, the cumulative time Δ for prescission neutron emission is identified with the time scale $\tau_{sm}^{(n)}$ for scission.

The resulting statistical distribution of the initial excitation energy $E_{CN}^*(\mathrm{LMT})$ is shown as an energy balance for $a=A/10\ \mathrm{MeV}^{-1}$ in Fig. 12. The prescission multiplicity for charged particle emission increases with LMT in a way that in the central collisions only about 50% of E_{CN}^* is spent on neutron emission and preferentially in the later part of the deexcitation chain. This is why the apparent temperatures T_{pre} fall behind $T_{\mathrm{eq}}(E_{CN}^*)$. On these grounds the temperatures $T_{sm}=\frac{2}{3}\bar{E}_n$ deduced from the averaged kinetic energy of the prescission neutrons as calculated with the statistical model should equal $T_{\mathrm{pre}}(E_{CN}^*)$ rather than $T_{\mathrm{eq}}(E_{CN}^*)$; the opposite, however, is the case (cf. Table V). It indicates that the statistical model applied might[67] overestimate the kinetic energies of evaporated particles, e.g., due to the fact that actually less intrinsic excitation is available because the reaction system is not spherical but deformed on its way toward scission.[44]

According to Fig. 12, M_{pre} is systematically higher for $^{32}S+^{232}Th$ than for $^{32}S+^{197}Au$ because the charged particle evaporation is less competitive. The calculated postscission multiplicities exceed those for $^{32}S+^{197}Au$, too, due to the higher value Q_{eff} that supplements the intrinsic excitation once the scission is completed. The absolute numbers agree well with the experimental results for symmetric fission. Altogether this energy balance yields satisfying agreement with the results of the multiple source fit and must be considered another support for Eq. (5) used to determine $E_{CN}^*(\mathrm{LMT})$ with $E_{\mathrm{PE}}=0$, and insofar also for the reliability of the scission times derived for reaction systems starting the descent towards scission from an excitation E_{CN}^*.

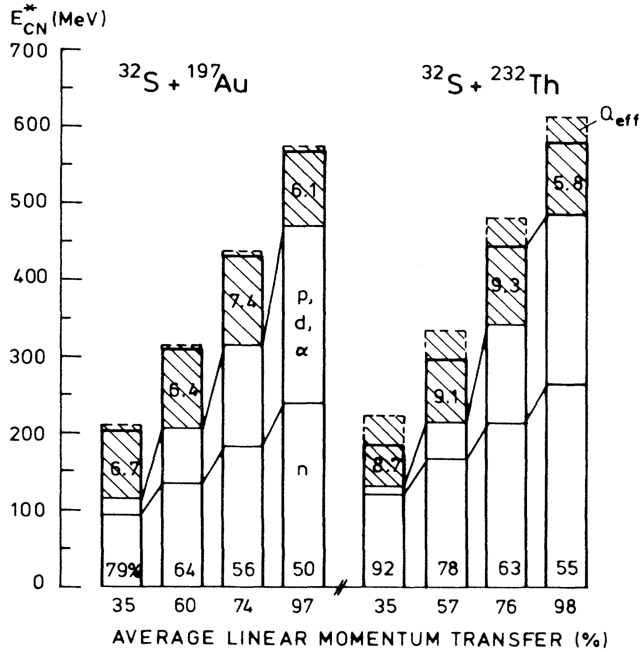

FIG. 12. Energy balance in the four LMT classes under study. The solid columns give E_{CN}^* following incomplete fusion, Eq. (5); the bottom fraction (also given in %) is carried away by prescission neutrons, the medium section by charged particles. The hatched part including a contribution of the effective Q value (i.e., mass difference for symmetric fragmentation minus TKE) is left for the postscission phase; the numbers give the calculated neutron multiplicities M_{post}.

B. Prescission times

According to Refs. 2 and 9 the effective fusion-fission lifetime for first charge fission is given by

$$\tau_f=\tau_{\mathrm{stat}}+0.5\tau_t+\tau_{ss}\ , \tag{14}$$

where τ_{stat} is the mere decay width contribution of the statistical model according to Eq. (10), τ_t the transient time to transform the initial reaction system by coupling of collective to particle degrees of freedom to a quasistatic distribution including the saddle-point configurations, and τ_{ss} the time needed to descend from the saddle to the scission point. Application of the neutron clock of Eq. (13) requires the knowledge of the number of neutrons M_{pre} minus the statistical model contribution resulting during τ_{stat}. For the reaction systems under study, τ_{stat} is much[12] smaller than τ_f and therefore $\tau_{sm}^{(n)}$ obtained from Eq. (13) with the full value M_{pre} can be used to determine the dynamical time scale of the transient phenomenon referred to with the second plus third term in Eq. (14).

For reaction systems that are not trapped behind a fission barrier (i.e., fast fission as contrasted to fusion-fission[68]), the statistical fission width Γ_f is infinite and the neutron clock measures directly the time scale for the transport of the nuclear fission degree of freedom over the fission barrier to the scission point, whereas fusion-fission also receives contributions from prescission neutron emission in statistical competition to fission. Therefore Eq. (13) then represents the minimum scission time scale.

The calculations of $\tau_{sm}^{(n)}$ were performed with the energy independent level-density parameters $a=A/k$

with[36,66] $k=8$, 10, and 13 MeV; a representative result is shown in Fig. 13 for the 74% LMT bin. The scission time scales deduced by means of the experimental results for M_{pre} overlap within the uncertainties originating from those ($\pm\Delta M_{\text{pre}}$) of M_{pre}. This applies for all other LMT bins of both reactions ^{32}S+^{197}Au,^{232}Th as well. Therefore the discussion will be restricted to the results obtained with $a = A/10\ \text{MeV}^{-1}$ as in Ref. 6.

Figure 13 demonstrates that $\tau_{sm}^{(n)}$ increases exponentially with the number of prescission neutrons such that the absolute times are essentially determined by the last two neutrons. The uncertainty ΔM_{pre} roughly corresponds to a factor of 2 on the time scale. The resulting time scales τ_f range from 5×10^{-21} s to 3×10^{-20} s depending on the reaction system, the mass split, and the LMT. These dependencies are less prone to the absolute values of the

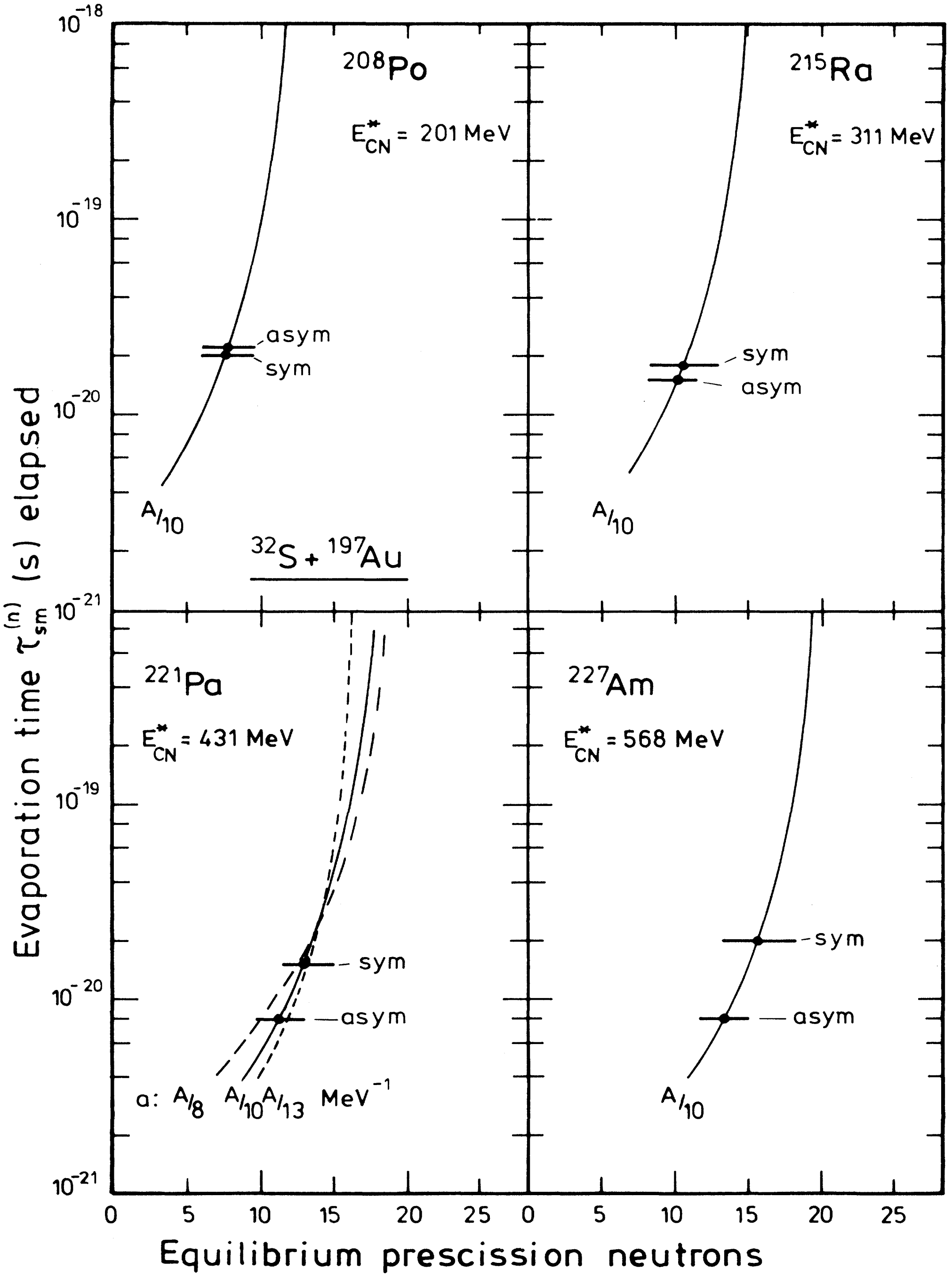

FIG. 13. Cumulative evaporation times (lines) calculated with a statistical model and the level-density parameters a indicated for the reaction systems following incomplete fusion of ^{32}S+^{197}Au. The horizontal bars give the experimental values M_{pre} with uncertainties for symmetric and asymmetric mass splits.

time scales and show smooth trends with deviations only in the lowest LMT bin; the latter can most probably be traced back to the fact that the excitation energies E^*_{CN}(LMT) for these bins are least accurate on an absolute scale due to the evaluation with Eq. (5) and their centroids being least representative for the bin.

The first result is that for symmetric fragmentations $\tau_f \approx 2\times10^{-20}$ s and does not depend on the LMT; the dynamical time scale is not extended with the amount of linear momentum and kinetic energy brought into the reaction system by the projectile participant. This is not unexpected, because on one hand τ_f seems to be dominated by τ_{ss} (Ref. 12) and τ_{ss} will depend on the mass at scission. This mass varies only moderately with LMT, because in first order the additional mass of the participant is canceled by the evaporation losses as a consequence of the growing internal excitation.[36] The same result is obtained for ^{32}S+^{232}Th, however with slightly higher absolute values $\tau_f \approx 3\times10^{-20}$ s as can be read from the upper part of Fig. 14.

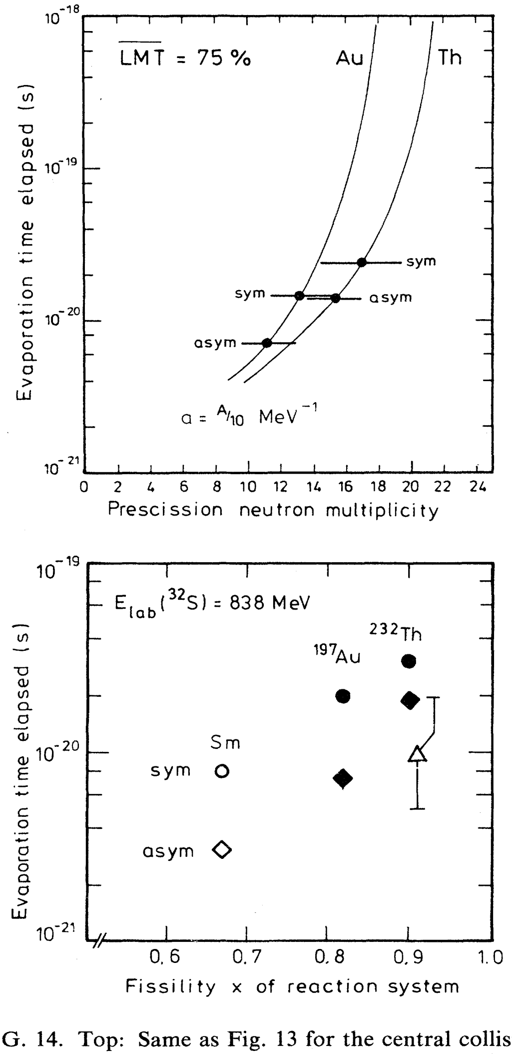

FIG. 14. Top: Same as Fig. 13 for the central collision window LMT=74% (76%) and the reactions ^{32}S+^{197}Au (^{32}S+^{232}Th). Bottom: Cumulative evaporation times versus fissility x of the reaction system for symmetric and asymmetric mass splits obtained with $a = A/10$ MeV^{-1} for the highest LMT bins. Data for ^{32}S+^{144,154}Sm are from Ref. 6; also shown (triangle) is the result (Ref. 8) for peripheral collisions ^{40}Ar+^{232}Th with 30 MeV/u.

Our second finding is that τ_f is systematically higher for symmetric than for the corresponding asymmetric fragmentations. Similar differences in time scales have been found in Ref. 3, and in particular for the fission following the reaction of 838-MeV projectiles ^{32}S with ^{144,154}Sm.[6] It was speculated in context with Fig. 7 that the symmetric mass splits are associated with more central collisions and therefore result from fission of a composite system that is equilibrated in energy and mass and characterized by lower angular momenta and accordingly higher fission barriers $V_B(l)$. In contrast, asymmetric mass splits originate more from peripheral collisions with higher angular momenta and partly from systems with vanishing[45,68] barriers $V_B(l)$ such that the time scale is dominated by fast fission. Of course there will be an overlap of fusion-fission, fast fission, and quasifission[69] as contributing reaction mechanisms. Support for the assumption of shorter time scales in peripheral collisions comes from a study[8] of fission following exclusively peripheral collisions of ^{40}Ar+^{232}Th at a bombarding energy of 30 MeV/u; there a dynamical time scale 0.5–2.0$\times10^{-20}$ s—which, however, was attributed more to τ_t—was derived. The comparison [cf. Fig. 14(b)] shows that this time scale is again shorter than the one for the asymmetric mass splits in ^{32}S+^{232}Th. It must be pointed out, however, that our data are not considered a conclusive link from asymmetric fragmentation to peripheral collisions.

Finally, it is instructive to consider the time scales deduced in this work as well as those from Refs. 6 and 8 as a function of the fissility x of the reaction system [Fig. 14(b)]. There is a clear trend of increasing time scales $\tau^{(n)}_{sm}$ or τ_f with x. Its attribution to either τ_t or τ_{ss} is model dependent. If it were due to the transient time τ_t, it would indicate the fission probability to be increasingly suppressed.[70] On the other hand, it supplements the speculation[15] for the saddle-to-scission time τ_{ss} to increase with x. This would indicate a growing difference between the deformations at the saddle and the scission point, respectively, either because the saddle point moves towards more compact shapes or because the heavier system is more elongated at scission.

VI. SUMMARY

Fission of the reaction systems ^{32}S+^{179}Au and ^{32}S+^{232}Th has been studied with 26.2-MeV/u projectiles by measuring in planar geometry coincidences of two heavy fragments with neutrons. The LMT has been obtained from the fragment velocity vectors and converted into the excitation energies E^*_{CN}(LMT) in the massive transfer approach. The neutron energy spectra have been unfolded for consecutive bins of LMT, mass split, and TKE into contributions of four (preequilibrium, prescission, and two fragments) moving sources with isotropic, Maxwellian emission characteristics. The main results of our data analysis are as follows.

(1) The most probable LMT in central collisions of about 75% corresponds to a transferred momentum of 168 MeV/*c* per projectile nucleon. The LMT distribution exhibits a second component of peripheral collisions that is more pronouced for ^{32}S$+^{232}$Th due to the higher fissility. The cross sections for fission in central collisions amount to 40–50 % of the total reaction cross sections. Complete fusion accounts for less than 10% of the fission yield. The detectable fraction of nonbinary fragmentations is well below 10%.

(2) For both reactions and in all LMT bins about 4 preequilibrium neutrons are emitted per fission; they stem from sources moving with 50% of the beam velocity and faster. Their multiplicities and energies are well reproduced by the BME model calculation that supports also the excitation energy E_{CN}^*(LMT) ascribed to reaction systems following incomplete fusion.

(3) Prescission neutron multiplicities increase with LMT in proportion to E_{CN}^*(LMT), whereas the postscission multiplicities remain constant at a level of 6–8 neutrons (for ^{23}Th two neutrons more due to a higher value Q_{eff}). These numbers as well as the temperature parameters obtained for the fragment sources imply that scission takes place when the elongated system has cooled down to 50–60 MeV of intrinsic excitation.

(4) A statistical model calculation starting from an initial excitation energy E_{CN}^*(LMT), and with the fission competition being deferred until the experimental prescission neutron multiplicity is reached, can explain the distribution of E_{CN}^*(LMT) between the competing channels of neutron and charged particle evaporation and the fraction remaining at scission. One minor discrepancy arises between the apparent temperature parameters $T_{\text{pre}}(E_{CN}^*)$ and the calculated ones, $T_{sm}(E_{CN}^*)$, the latter being higher; it emphasizes that the reaction is inadequately described with compound nuclei remaining spherical throughout the deexcitation and transition to the scission point.

(5) Accumulation of the times elapsed for the evaporation of all prescission neutrons leads to a time scale showing that fission of the systems under study is an inherently slow process of 5×10^{-21}–3×10^{-20} s duration. A comparison of the fission times on a relative scale indicates that they are not significantly dependent on E_{CN}^*(LMT). It is found that fission proceeds faster for asymmetric mass splits than for symmetric ones. For both types of mass split the fission time scale increases with the fissility *x* of the reaction system, which may be indicative of an increasing distance between saddle and scission point.

ACKNOWLEDGMENTS

The collaborators from the University of Hamburg gratefully acknowledge the support from the technical staff of the VICKSI laboratory. We thank Dr. M. Blann for providing us with the BME calculations and Dr. Folger (GSI) for target preparation. This work was financially supported by the Bundesministerium für Forschung und Technologie (Contracts No. 06 HH-175 and F+E 151/531/8959).

---

[1] D. J. Hinde, D. Hilscher, and H. Rossner, Nucl. Phys. **A502**, 497c (1989), and references therein.

[2] D. J. Hinde, H. Ogata, M. Tanaka, T. Shimoda, N. Takahashi, A. Shinohara, S. Wakamatsu, K. Katori, and H. Okamura, Phys. Rev. C **39**, 2268 (1989).

[3] G. F. Peaslee, N. N. Ajitenand, J. M. Alexander, D. Guerreau, R. Lacey, L. C. Vaz, M. Kaplan, M. Kildir, D. J. Moses, D. Logan, and M. S. Zisman, Phys. Rev. C **38**, 1730 (1988).

[4] M. Thoennessen, D. R. Chakrabarty, M. G. Herman, R. Butsch, and P. Paul, Phys. Rev. Lett. **59**, 2860 (1987).

[5] J. Pochodzalla, R. J. Charity, U. Lynen, H. Sann, W. Trautmann, and R. Trockel, Phys. Rev. C **40**, 2918 (1989).

[6] D. Hilscher, H. Rossner, B. Cramer, U. Jahnke, M. Lehmann, E. Schwinn, M. Wilpert, T. Wilpert, H. Frobeen, E. Mordhorst, and W. Scobel, Phys. Rev. Lett. **62**, 1099 (1989).

[7] M. Strecker, R. Wien, P. Plischke, and W. Scobel, Phys. Rev. C **41**, 2172 (1990).

[8] E. M. Eckert, A. Kühmichel, J. Pochodzalla, K. D. Hildenbrand, U. Lynen, W. F. J. Müller, H. J. Rabe, H. Sann, H. Stelzer, W. Trautmann, R. Trockel, R. Wada, C. Cerruti, P. Lhénoret, R. Lucas, C. Mazur, C. Ngô, M. Ribrag, E. Tomasi, A. Demeyer, and D. Guinet, Phys. Rev. Lett. **64**, 2483 (1990).

[9] P. Grangé, S. Hassani, H. A. Weidenmüller, A. Gavron, J. R. Nix, and A. J. Sirk, Phys. Rev. C **34**, 209 (1986).

[10] M. Blann, Phys. Rev. C **31**, 1245 (1985).

[11] W. Scobel, E. Mordhorst, M. Strecker, and R. Caplar, in *Proceedings of the 6th International Adriatic Conference on Nuclear Physics, Dubrovnik, 1987,* edited by N. Cindro, W. Greiner, and R. Caplar (World Scientific, Singapore, 1987), p. 267.

[12] J. Galin, Nucl. Phys. **A488**, 297c (1988).

[13] A. Gavron, Nucl. Phys. **A502**, 515c (1989).

[14] R. Nix, Nucl. Phys. **A502**, 609c (1989).

[15] J. O. Newton, J. D. Hinde, R. J. Charity, J. R. Leigh, J. J. M. Bokhorst, A. Chatterjee, G. S. Foote, and S. Ogaza, Nucl. Phys. **A483**, 126 (1988).

[16] N. Carjan, A. Sierk, and R. Nix, Nucl. Phys. **A452**, 381 (1986).

[17] M. Fatyga, K. Kiwatkowski, V. E. Viola, C. B. Chitwood, D. J. Fields, C. K. Gelbke, W. G. Lynch, J. Pochodzalla, M. B. Tsang, and M. Blann, Phys. Rev. Lett. **55**, 1376 (1985).

[18] C. Volant, M. Conjeaud, S. Harar, M. Mostefai, E. C. Pollacco, Y. Cassagnou, R. Dayras, R. Legrain, G. Klotz-Engmann, and H. Oeschler, Phys. Lett. B **195**, 22 (1987).

[19] H. Rossner, D. Hilscher, D. J. Hinde, B. Gebauer, M. Lehmann, M. Wilpert, and E. Mordhorst, Phys. Rev. C **40**, 2629 (1989).

[20] G. La Rana, G. Nebbia, E. Tomasi, C. Ngô, X. S. Chen, S. Leray, P. Lhenoret, R. Lucas, C. Mazur, M. Ribrag, C. Cerruti, S. Chiodelli, A. Demeyer, D. Guinet, J. L. Charvet, M. Morjean, A. Peghaire, Y. Pranal, L. Sinopoli, J. L. Uzureau, and R. de Swiarski, Nucl. Phys. **A407**, 233 (1983).

[21] D. X. Jiang, H. Doubre, J. Galin, D. Guerreau, E. Piasecki, J. Pouthas, A. Sokolov, B. Cramer, G. Ingold, U. Jahnke, E. Schwinn, J. L. Charvet, J. Frehaut, B. Lott, C. Magnago, M. Morjean, Y. Patin, Y. Pranal, J. L. Uzureau, B. Gatty, and D. Jacquet, Nucl. Phys. **A503**, 560 (1989).

[22] R. Trockel, K. D. Hildenbrand, U. Lynen, W. F. J. Müller, H. J. Rabe, H. Sann, H. Stelzer, W. Trautmann, R. Wada, E. Eckert, P. Krenz, A. Kühmichel, J. Pochodzalla, and D.

Pelte, Phys. Rev. C **39**, 729 (1989).

[23] M. Morjean, J. Frehaut, D. Guerreau, J. L. Charvet, G. Duchene, H. Doubré, J. Galin, G. Ingold, D. Jacquet, U. Jahnke, D. X. Jiang, B. Lott, C. Magnago, Y. Patin, J. Pouthas, Y. Pranal, and J. L. Uzureau, Phys. Lett. B **203**, 215 (1988).

[24] R. Dayras, A. Pagano, J. Barrette, B. Berthier, D. M. de Castro Rizzo, E. Chavez, O. Cisse, R. Legrain, M. C. Mermaz, E. C. Pollacco, H. Delagrange, W. Mittig, B. Heusch, R. Coniglione, G. Lanzano, and A. Palmeri, Nucl. Phys. **A460**, 299 (1986).

[25] A. Gavron, A. Gayer, J. Boissevain, H. C. Britt, T. C. Awes, J. R. Beene, B. Cheynis, D. Drain, R. L. Ferguson, F. E. Obenshain, F. Plasil, G. R. Young, G. A. Petitt, and C. Butler, Phys. Rev. C **35**, 579 (1987).

[26] H. W. Schmitt, W. E. Kiker, and C. W. Williams, Phys. Rev. B **137**, B837 (1973).

[27] E. Weissenberger, A. Oed, F. Gönnewein, and H. Faust, Nucl. Intrum. Methods **A248**, 506 (1986).

[28] K. Paasch, H. Krause, and W. Scobel, Nucl. Instrum. Methods **221**, 558 (1984).

[29] H. O. Neidel and H. Henschel, Nucl. Instrum. Methods **178**, 137 (1980).

[30] M. Strecker, Ph.D. thesis, University of Hamburg, 1990.

[31] E. Mordhorst, Ph.D. thesis, University of Hamburg, 1990.

[32] T. N. Taddeucci, ATTENE—Program for Neutron Flux Attenuation (Los Alamos National Laboratory, Los Alamos, NM, 1987); private communication.

[33] G. Dietze and H. Klein, Physikalisch-Technische Bundesanstalt Braunschweig Report PTB-ND-22, 1982.

[34] R. A. Cecil, B. D. Anderson, and R. Madey, Nucl. Instrum. Methods **161**, 439 (1979).

[35] D. Hilscher, H. Rossner, A. Gamp, U. Jahnke, B. Cheynis, B. Chambon, D. Drain, C. Pastor, A. Giorni, C. Morand, A. Dauchy, P. Stassi, and G. Petit, Phys. Rev. C **36**, 208 (1987).

[36] K. Hagel, D. Fabris, P. Gonthier, H. Ho, Y. Lou, Z. Majka, G. Mouchanty, M. N. Nayboodiri, J. B. Natowitz, G. Nebbia, R. P. Schmitt, G. Viesti, R. Wada, and B. Wilkins, Nucl. Phys. **A486**, 429 (1988).

[37] G. Klotz-Engmann, H. Oeschler, J. Stroth, E. Kankeleit, Y. Cassagnou, M. Conjeaud, R. Dayras, S. Harar, R. Legrain, E. C. Pollacco, and C. Volant, Nucl. Phys. **A499**, 392 (1989).

[38] D. J. Hinde, R. J. Charty, G. S. Foote, J. R. Leigh, J. O. Newton, S. Ogaza, and A. Chatterjee, Nucl. Phys. **A452**, 550 (1986).

[39] A. H. Wapstra and K. Bos, At. Data Nucl. Data Tables **17**, 474 (1976).

[40] S. Cohen, F. Plasil, and W. J. Swiatecki, Ann. Phys. (N.Y.) **82**, 557 (1974).

[41] M. Conjeaud, S. Harar, M. Mostefai, E. C. Pollacco, C. Volant, Y. Cassagnon, R. Dayras, R. Legrain, H. Oeschler, and F. Saint-Laurent, Phys. Lett. **159B**, 244 (1985).

[42] V. E. Viola, Jr., K. Kwiatkowski, and M. Walker, Phys. Rev. C **31**, 1550 (1985).

[43] G. Klotz-Engmann, H. Oeschler, E. Kankeleit, Y. Cassagnon, M. Conjeaud, R. Dayras, S. Harar, M. Mostefai, R. Legrain, E. C. Pollacco, and C. Volant, Phys. Lett. B **187B**, 245 (1987).

[44] D. Jaquet, G. F. Peaslee, J. M. Alexander, B. Borderie, E. Duek, J. Galin, D. Gardes, C. Grégoire, D. Guerreau, H. Fuchs, M. Lefort, M. F. Rivet, and X. Tarrago, Nucl. Phys. **A511**, 195 (1990); D. Jaquet, J. Galin, B. Borderie, D. Gardes, D. Guerreau, M. Lefort, F. Monnet, M. F. Rivet, X. Tarrago, E. Duek, and J. M. Alexander, Phys. Rev. C **32**, 1594 (1985).

[45] A. J. Sierk, Phys. Rev. C **33**, 2039 (1986).

[46] V. E. Viola, Nucl. Phys. **A502**, 531c (1989).

[47] L. E. Tubbs, J. R. Birkelund, J. R. Huizenga, D. Hilscher, U. Jahnke, H. Rossner, and B. Gebauer, Phys. Rev. C **32**, 214 (1985).

[48] J. Galin, J. L. Charvet, B. Cramer, E. Crema, H. Doubré, J. Frehaut, B. Gatty, D. Guerreau, G. Ingold, D. Jacquet, U. Jahnke, D. X. Jiang, B. Lott, C. Magnago, M. Morjean, Y. Patin, E. Piasecki, J. Pouthas, F. Saint-Laurent, E. Schwinn, A. Sokolov, and X. D. Wang, in *Proceedings of the Symposium on Nuclear Dynamics and Nuclear Disassembly,* Dallas, Texas, 1989, edited by J. B. Natowitz (World Scientific, Singapore, 1989), p. 320.

[49] W. W. Wilcke, J. R. Birkelund, H. J. Wollersheim, A. D. Hoover, J. R. Huizenga, W. U. Schröder, and L. E. Tubbs, At. Data Nucl. Data Tables **25**, 389 (1980).

[50] W. U. Schröder and J. R. Huizenga, Nucl. Phys. **A502**, 473c (1989).

[51] D. Hilscher, J. R. Birkelund, A. D. Hoover, W. U. Schröder, W. W. Wilcke, J. R. Huizenga, A. C. Mignerey, K. L. Wolf, H. F. Breuer, and V. E. Viola, Jr., Phys. Rev. C **20**, 576 (1979).

[52] B. E. Watt, Phys. Rev. **87**, 1037 (1952).

[53] K. J. Le Couteur and D. W. Lang, Nucl. Phys. **13**, 32 (1959).

[54] D. Hilscher, in *Proceedings of the Specialists Meeting on Preequilibrium Nuclear Reactions, Semmering, Austria, 1988,* edited by B. Strohmaier (OECD Nuclear Energy Agency, Paris, 1988), p. 245.

[55] M. Korolija, N. Cindro, and R. Caplar, Phys. Rev. Lett. **60**, 193 (1988).

[56] E. Holub, D. Hilscher, G. Ingold, U. Jahnke, H. Orf, and H. Rossner, Phys. Rev. C **28**, 252 (1983).

[57] D. J. Hinde, D. Hilscher, and H. Rossner, private communication; and (unpublished).

[58] W. P. Zank, D. Hilscher, G. Ingold, U. Jahnke, M. Lehmann, and H. Rossner, Phys. Rev. C **33**, 519 (1986).

[59] M. Korolija, N. Cindro, R. Caplar, R. L. Auble, J. B. Ball, and R. L. Robinson, Z. Phys. A **327**, 237 (1987).

[60] E. Fabrici, E. Gadioli, and E. Gadioli Erba, Phys. Rev. C **40**, 459 (1989).

[61] M. Blann and B. Remington, Phys. Rev. C **37**, 2231 (1988).

[62] K. Knoche, L. Sprute, E. Mordhorst, W. Scobel, M. Strecker, B. Cramer, B. Gebauer, D. Hilscher, U. Jahnke, and E. Schwinn (unpublished).

[63] Z. Fraenkel, A. Breskin, R. Chechik, S. Wald, R. Abegg, H. W. Fielding, P. Kitching, S. T. Lam, G. C. Neilson, W. C. Olsen, and J. Uegaki, Phys. Rev. C **41**, 1050 (1990).

[64] D. Hilscher, D. J. Hinde, and H. Rossner, in *Proceedings of the Texas A&M Symposium on Hot Nuclei, College Station, Texas, 1987,* edited by S. Shlomo, R. P. Schmitt, and J. B. Natowitz (World Scientific, Singapore, 1988), p. 193.

[65] E. Cheifetz, Z. Fraenkel, J. Galin, M. Lefort, J. Péter, and X. Tarrago, Phys. Rev. C **2**, 256 (1970).

[66] M. Gonin, L. Cooke, B. Fornal, P. Gonthier, M. Gui, Y. Lou, J. B. Natowitz, G. Nardelli, G. Nebbia, G. Prete, R. P. Schmitt, B. Srivaslava, W. Turmel, D. Utley, H. Utsunomiya, G. Viesti, R. Wada, B. Wilkins, and R. Zanon, Nucl. Phys. **A495**, 139c (1989).

[67] D. Hilscher, Nucl. Phys. **A471**, 77c (1987).

[68] C. Gregoire, C. Ngo, E. Tomasi, B. Remaud, and F. Scheuter, Nucl. Phys. **A387**, 37c (1982).

[69] J. Toke, R. Bock, G. X. Dai, A. Gobbi, S. Gralla, K. D. Hildenbrand, J. Kuzminski, W. J. F. Müller, A. Olmi, H. Stelzer, B. B. Back, and S. Bjornholm, Nucl. Phys. **A440**, 327 (1985).

[70] J. B. Natowitz, M. Gonin, M. Gui, K. Hagel, Y. Lou, D. Utley, and R. Wada, Phys. Lett. B **247**, 242 (1990).